Neuron

Article

Walking strides direct rapid and flexible recruitment of visual circuits for course control in *Drosophila*

Highlights

- HS cells receive stride-coupled signals via ascending neurons
- The stride-coupled signals reflect an internal motor context
- Motor context modulates HS cells at multiple timescales
- HS cells drive rapid steering depending on motor context

Authors

Terufumi Fujiwara, Margarida Brotas, M. Eugenia Chiappe

Correspondence

eugenia.chiappe@neuro.fchampalimaud.org

In brief

Fujiwara et al. show that HS cells, self-motion sensitive neurons in *Drosophila*, are modulated at different timescales by walking strides. The modulation recruits HS cells to adjust heading only during fast walking. This study provides a mechanistic link between body state and brain activity for the flexible control of locomotion.

Fujiwara et al., 2022, Neuron *110*, 2124–2138
July 6, 2022
https://doi.org/10.1016/j.neuron.2022.04.008

CellPress

CellPress
OPEN ACCESS

Neuron

Article

Walking strides direct rapid and flexible recruitment of visual circuits for course control in *Drosophila*

Terufumi Fujiwara,[1] Margarida Brotas,[1] and M. Eugenia Chiappe[1,2,*]
[1]Champalimaud Research, Champalimaud Centre for the Unknown, Lisbon 1400-038, Portugal
[2]Lead contact
*Correspondence: eugenia.chiappe@neuro.fchampalimaud.org
https://doi.org/10.1016/j.neuron.2022.04.008

SUMMARY

Flexible mapping between activity in sensory systems and movement parameters is a hallmark of motor control. This flexibility depends on the continuous comparison of short-term postural dynamics and the longer-term goals of an animal, thereby necessitating neural mechanisms that can operate across multiple timescales. To understand how such body-brain interactions emerge across timescales to control movement, we performed whole-cell patch recordings from visual neurons involved in course control in *Drosophila*. We show that the activity of leg mechanosensory cells, propagating via specific ascending neurons, is critical for stride-by-stride steering adjustments driven by the visual circuit, and, at longer timescales, it provides information about the moving body's state to flexibly recruit the visual circuit for course control. Thus, our findings demonstrate the presence of an elegant stride-based mechanism operating at multiple timescales for context-dependent course control. We propose that this mechanism functions as a general basis for the adaptive control of locomotion.

INTRODUCTION

Adaptive behavior—behavior that enhances survival in complex environments—depends on the capacity of the central nervous system to flexibly engage neural networks for motor control (Dickinson et al., 2000; Dürr, 2005; Wolpert and Ghahramani, 2000). Importantly, this flexibility operates according to internal contexts that can be defined by physiological needs (Augustine et al., 2020; Bargmann, 2012), past experience (Palmer and Kristan, 2011; Khan and Hofer, 2018; Maren et al., 2013), and by predictions of the state of the body given the behavioral goals. Because movement is rarely executed as intended without online adjustments (Shadmehr et al., 2010), the internal context defined by signals associated with behavioral goals and the current body state, here defined as "motor context," is critical for high-performance movement control. Motor context emerges from diverse streams of information across different timescales; however, how the central nervous system signals it to flexibly recruit circuits for online movement adjustments remains poorly understood (Figure 1A).

The emergence of an internal motor context likely depends on recurrent interactions between brain premotor centers and the spinal cord across different timescales (Figure 1A). Coupling of ascending signals in the mammalian brain to individual strides suggests that supraspinal circuits receive immediate information about the walking state (Orlovsky et al., 1999). However, the exact nature and function of these modulations remains unknown, partly due to the highly distributed structure of mammalian brain premotor circuits and to the limited understanding of how activity within these circuits contributes to walking. The compact central nervous system of *Drosophila melanogaster* provides a powerful model in which to study the mechanisms and timescales through which motor context emerges and impacts neural activity and walking control. Importantly, and in contrast to internal physiological states, signals related to the state of the body can be directly measured by quantitative analysis of behavior and neural physiology, thus allowing to dissect the nature of motor context and its effect on motor control. In insects, the posterior slope (PS, Figure 1B), a premotor region with strong multisensory convergence (Strausfeld and Bacon, 1983), provides output to several types of descending neurons (DNs) involved in steering (Namiki and Kanzaki, 2016; Rayshubskiy et al., 2020). The PS receives inputs from higher-order centers, such as the lateral accessory lobe (LAL), from the ventral nerve cord (VNC, the insect analog of the spinal cord) via ascending neurons (ANs), and from visual pathways, including the lobula plate (LP) (Figure 1B) (Namiki and Kanzaki, 2016; Pierantoni, 1976; Scheffer et al., 2020; Strausfeld, 1976). Therefore, neurons projecting to PS are likely involved in brain-body interactions for context-dependent motor control, but their activity has not been characterized at multiple timescales in relation to the task at play, behavioral goals, or the body state.

One class of such premotor neurons projecting to the PS is the population of horizontal system (HS) cells in the LP, visual motion sensitive neurons that are well poised to detect head and body

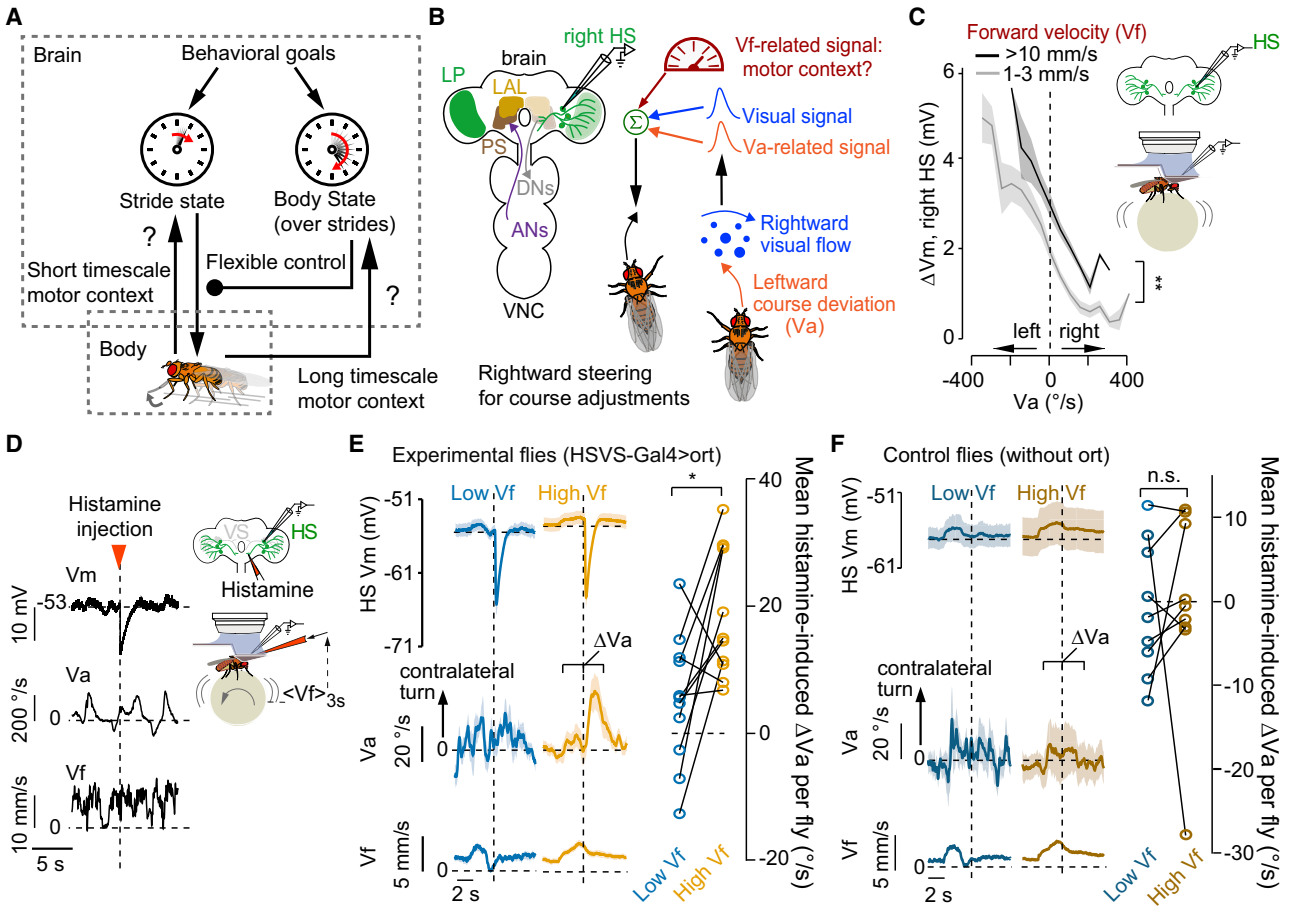

Figure 1. HS cells contribute to steering in high- but not low-speed walking bouts

(A) Schematic of brain-body interactions across timescales.

(B) Schematic of the anatomy (left) and physiological properties of HS cells during walking (right).

(C) Change in membrane potential (ΔVm) as a function of the angular velocity (Va) of the fly in walking bouts with low (gray) or high (black) forward velocity (Vf) ($p = 0.79$ for the slope; $p = 0$ for the offset difference between curves, grand mean ± SEM, $n = 556$ bouts from 9 flies, bootstrapping method).

(D) Conditional unilateral inhibition in HS cells (right). Example time series of Vm, Va, and Vf with a single histamine application in HS cells expressing the Ort histamine receptor.

(E) Left, Vm, Va, and Vf traces in experimental flies (grand mean ± SEM, $n = 11$ flies) triggered at histamine injection during low (blue) or high (orange) Vf. Right, mean histamine-induced change in Va (ΔVa) per fly. Lines connect the same individual ($p = 0.019$, $n = 11$ flies, the signed-rank test).

(F) Same as (E) but for controls ($p = 0.36$, $n = 9$ flies, signed-rank test).

See also Figure S1.

yaw rotations (Hausen, 1984; Schnell et al., 2010) and that are accessible to physiological recordings and manipulations during walking (Figure 1B) (Fujiwara et al., 2017; Kim et al., 2015; Schnell et al., 2014; Suver et al., 2012). Consistent with their proposed role on course and gaze stabilization, the activity of HS cells is suppressed in anticipation to voluntary rapid turns (Fenk et al., 2021; Kim et al, 2015, 2017; Cruz et al., 2021), suggesting that HS cells contribute to behavior in a task-specific manner. Rapid turns are only one of many maneuvers the fly executes while walking. More recently, we found that in the context of slower rotations during forward walking, HS cells respond to the direction of the angular velocity (Va) of the fly (Fujiwara et al., 2017) and integrate this extra-retinal information with visual motion signals to faithfully estimate body rotations (Figure 1B). Moreover, unilateral activation of HS cells promotes ipsilateral steering (Busch et al., 2018; Fujiwara et al., 2017; Haikala et al., 2013), suggesting a direct contribution to course control. However, at which timescales and in which motor contexts activity in HS cells is recruited for course control has not been explored yet. Interestingly, HS cell activity also correlates with the fly's forward velocity (Vf) (Fujiwara et al., 2017), but the function of this signal has remained unclear (Figure 1B). One possibility is that the speed-related signal provides information about motor context, either related to the behavioral goals of the fly ("run forward") or to the current state of the body ("walking at high speed"), or both. We therefore propose that this visuomotor circuit is very well suited to study the nature of motor context and its effect on neural activity and behavior.

Here, we combine whole-cell patch recordings in walking flies with optogenetics and targeted suppression of chemical

synapses to examine the emergence of motor context and its role on the mapping between neural activity dynamics and specific aspects of walking control. We show that a single source, the stride, operating at multiple timescales provides an elegant solution to flexibly engage a functional network in online movement adjustments within a continuous behavior that is rarely in steady state. These findings represent a general mechanism by which bidirectional interactions between the peripheral nervous system and brain visual circuits contribute to an adaptive and high-performance control of locomotion.

RESULTS

HS cells contribute to steering in a forward-velocity-dependent manner

HS cells are thought to contribute to course control when the fly actively maintains the direction of locomotion during walking at high speed (Figure 1B). If a Vf-related signal in HS cells functions as a motor context modulation, two properties should be observed. First, the selectivity of HS cells should not change with Vf. Second, manipulating HS-cell activity should lead to steering in a Vf-dependent manner. To test the first prediction, we examined the extra-retinal direction-selective properties of HS cells at different Vf by performing the whole-cell recordings of flies walking in darkness. We excluded visual stimulation in these experiments, since its presence influences the walking speed of the fly (Creamer et al., 2018). The activity of HS cells was selective to the fly's direction of rotations independent of Vf, but the cells were more depolarized under high versus low Vf (Figure 1C). Thus, Vf modulates the activity of HS cells without changing their tuning.

To test the second prediction, a Vf-dependent effect of the activity of HS cells on their behaviors, we leveraged previous work showing that unilateral activation induces ipsiversive rotations (Busch et al., 2018; Fujiwara et al., 2017) and reasoned that the opposite, unilateral silencing, should induce a contraversive rotation. To induce unilateral silencing, we expressed the histamine-gated chloride channel *ort* (Liu and Wilson, 2013) in HS cells and locally applied histamine at the right-side axon terminals in the PS, contingent on Vf (Figure 1D). Histamine application led to a prominent inhibition in right HS cells both at high and low Vf. However, in 9 out of 11 flies, the inhibition of HS cells led to an overt contraversive rotation only when flies walked at high Vf (Figure 1E). Importantly, the perturbation in neural activity and the effect on behavior was observed exclusively in experimental and not in control flies, in which HS cells did not exogenously express Ort (Figures 1F and S1A). Thus, these results cannot be explained by endogenous histamine receptor activity within the PS. Finally, the effect on behavior was not induced by inhibiting other neurons also labeled in the transgenic line (Figures S1B and S1C). We conclude that the Vf-related modulation in HS cells represents a motor context that flexibly recruits the neurons' activity to steering adjustments.

A Vf-related signal modulates HS cell activity across multiple timescales

In a continuous behavior such as walking, Vf can fluctuate at different timescales, reflecting either slow (over seconds) changes in motor programs or behavioral goals or faster fluctuations (at a stride timescale) in reactive forces due to inevitable perturbations (Figure 1A) (Chun et al., 2021; DeAngelis et al., 2019; Mendes et al., 2013). Thus, if HS cells are recruited for rapid steering adjustments, their activity should not only be modulated over seconds, reflecting the overall state of Vf, but also at timescales of a stride. When the fly occasionally maintained a stable heading with high Vf and low Va during spontaneous walking (Figures 2A and 2B, gray shadow), the activity of HS cells mapped onto these virtual straight paths revealed fast periodic oscillations (Figure 2C). This observation suggested the presence of a fast modulation by Vf, an idea we tested by calculating the coherence between neural activity dynamics (Vm) and Vf or Va, a measure of power transfer between signals. At high-speed walking frequencies on the ball, with a period of about 160 ms (>5 Hz), the coherence was dominated by Vf, while at lower frequencies (<5 Hz) it was dominated by Va (Figure 2D). These results show that Vf-related signals are present in the activity dynamics of HS cells at both a stride timescale (>5 Hz) and over seconds (Figure 1).

An optogenetic paradigm to study modulation of HS cells by Vf across multiple timescales

Because spontaneous walking on the ball is variable, we developed an optogenetics-based paradigm to promote high-speed walking (Figures 2E and 2F). We expressed the light-gated cation channel CsChrimson in interneurons promoting forward runs, the bolt protocerebral neurons (BPNs, Figure 2E) (Bidaye et al., 2020). To prevent any visual response that might confound the Vf-related modulation, we used blind flies (Bloomquist et al., 1988). BPN activation induced high-speed walking with low Va (absolute mean ± SEM = 73.6 ± 3.0°/s, n = 19 flies). We will refer to this induced walking as "opto-runs." Similar to that in spontaneous walking, during opto-runs HS-cell activity co-varied at high frequencies (5–10 Hz) with Vf and at low frequencies with Va. In addition, Va displayed a high-frequency (5–10 Hz) component (Figure 2G), which we will revisit later (Figure 5). Under visual feedback, opto-runs displayed lower course variability relative to darkness in flies with normal sight (Figure S2A), suggesting that these high-speed runs reflect an (induced) intention to walk straight (Cruz et al., 2021). Therefore, unexpected deviations from a stable course should recruit activity in steering-control networks, including HS cells. Together, these observations show that the opto-run paradigm is suitable to examine the interaction between activity in HS cells and strides during high-speed walking.

HS cell activity is phase locked to the walking stride cycle

The correlation between Vm and Vf at high frequencies suggests that HS cells are modulated at stride timescale. To determine the relationship between the stride cycle and activity in HS cells, we tracked the three legs from the left side (Mathis et al., 2018) and recorded in simultaneous the membrane potential of HS cells (Vm), Vf and Va during opto-runs (Figures 3A, S2B, and S2C; Video S1). Vm was strongly coupled to the stride cycle (Figures 3B, S2D, and S2E), with a peak-to-trough amplitude ranging from 2 to 6 mV, which was never observed in quiescence (Figure 3C). Hereafter, to analyze the phase relation between the oscillatory dynamics in HS

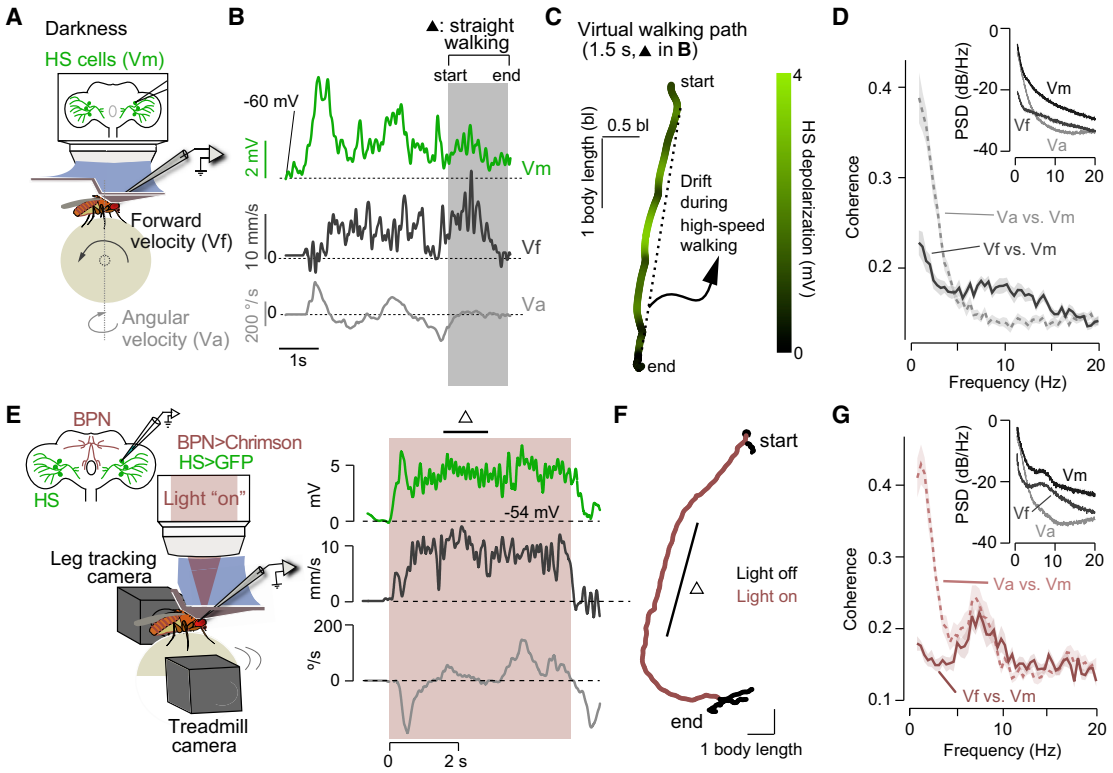

Figure 2. HS cells and the forward velocity of the fly oscillate at high frequencies during fast walking

(A) Schematic of the experimental configuration.

(B) Example traces of Vm (green, right HS cell), Vf (black), and Va (gray). The shade highlights a segment with high Vf and low Va (i.e., straight walking).

(C) Virtual walking path from the straight walking segment in (B). Color code: Vm activity.

(D) Coherence between Va and Vm (dashed), or Vf and Vm (solid, grand mean ± SEM, n = 25 fly cell pairs). The inlet shows the power spectral density of Vm, Vf, and Va.

(E) Left, schematic of the opto-run paradigm. Right, example traces of Vm (green, right HS cell), Vf (black), and Va (gray) in opto-runs (red shade).

(F) The virtual path for traces in (E). Δ: straight segment.

(G) Same as (D) but in opto-runs (n = 19 fly cell pairs).

cells, Vf, and the stride cycle, we used $Vm_{|5\ Hz}$, the high-frequency component of Vm (Figure 2; see STAR Methods).

$Vm_{|5\ Hz}$ oscillations were also observed in spontaneous walking under visual feedback (Figure 3D), and both in spontaneous- and opto-runs, each leg displayed a specific phase relation with $Vm_{|5\ Hz}$, which depended on the neural recording side (Figures 3D–3F and S2D–S2F). For example, the early stance phase of the left front leg coincided with the peak of the right side and the trough of the left side HS cells' oscillations (Figures 3D–3F). The phase relation of the front versus middle legs with the contralateral $Vm_{|5\ Hz}$ was shifted by about 120° (Figure 3E), consistent with a tetrapod-like gait configuration (DeAngelis et al., 2019; Mendes et al., 2013; Wosnitza et al., 2013). The hind leg movement was less correlated to $Vm_{|5\ Hz}$ (Figures 3E and S2G–S2I) and therefore was not the focus of further analysis. Altogether, these observations revealed a fixed relation between a specific leg's stride cycle and the contralateral $Vm_{|5\ Hz}$, and an antiphase relation between the activity of left and right HS cells.

The oscillations in $Vm_{|5\ Hz}$ could originate from a mechanical coupling between forces exerted by legs and brain motion, or as a direct consequence of BPN activation. To address the first possibility, we recorded the activity in the vertical system (VS) cells, which reside close by HS cells but display no modulation by Vf (Fujiwara et al., 2017). We found that their activity was not coupled to the stride cycle (Figures S2J–S2L). To test whether activation of BPNs directly induces oscillations in HS cells, we momentarily decoupled BPN activity from walking by stopping the airflow of the ball while activating BPNs. Stopping the ball induced uncoordinated leg movements, which were revealed by a decrease in the periodicity of the autocorrelation of the leg signal ("leg motion coupling," Figure S3). When walking was interrupted, Vm oscillations (for comparison, measured as the autocorrelation of the Vm signal, "Vm coupling") decreased (Figure S3B). Overall, Vm coupling was strongly correlated with leg motion coupling (Figures S3A–S3C), indicating that activity of BPNs or postsynaptic neurons per se was not driving the rhythmic neural activity. Rather, the oscillations in HS cells may reflect leg kinematic parameters, such as joint positions. Indeed, HS cells were more depolarized when the femur-tibia or tibia-tarsus joint position at stance onset was more anterior (Figures S3D and S3E). These results suggest that oscillations in HS cells originate from periodic leg movements.

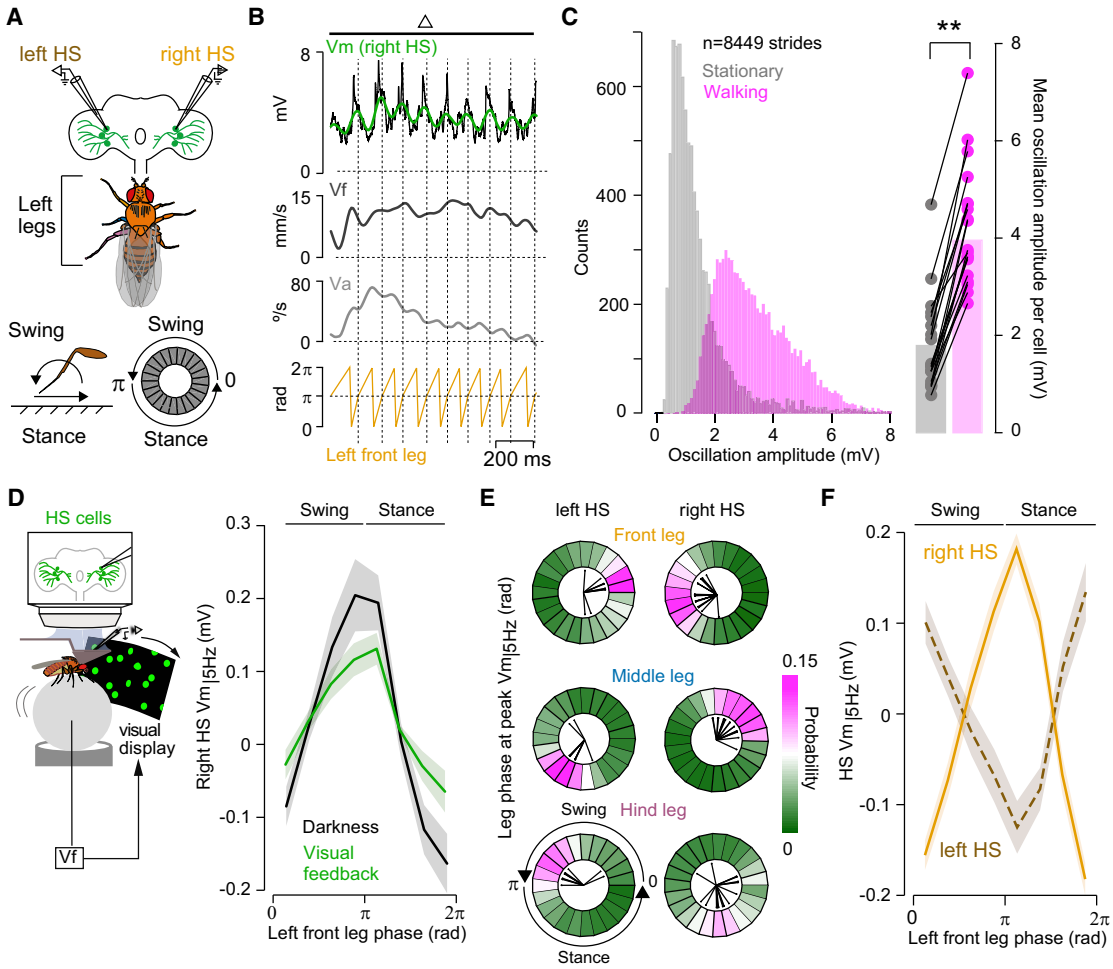

Figure 3. High-speed walking bouts reveal specific phase relations between neural activity and the stride cycle

(A) Schematic of experimental configuration and definitions.

(B) Example traces of Vm (black: raw, green: filtered), Vf, Va, and the left front leg phase, triggered at the stance onset.

(C) Left, distribution of the magnitude of the oscillations during walking (magenta) versus quiescence (gray) across 19 fly-cell pairs. Right, mean amplitude of oscillations during walking (3.95 ± 0.29 mV) and quiescence (1.79 ± 0.22 mV) ($p = 0.00013$, $Z = 3.823$, the signed-rank test).

(D) Left, schematic of the experimental configuration. Right, tuning of right HS cells ($Vm_{|5\ Hz|}$) to the stride cycle of the left front leg during spontaneous walking in darkness (black) and under visual feedback (green, n = 8 fly cell pairs, grand mean ± SEM).

(E) Probability distributions of the phase of the stride cycle at the peak of $Vm_{|5\ Hz|}$ oscillation (contralateral/ipsilateral cells, 4,182–4,747/1,937–2,269 strides, n = 19/11 fly cell pairs). Black lines indicate the mean per cell.

(F) $Vm_{|5\ Hz|}$ as a function of the stride cycle of the left front leg during opto-runs (right cells: solid orange, n = 19 fly cell pairs; left cells: dashed maroon, n = 11 fly cell pairs).

See also Figures S2–S4 and Video S1.

A simple model suggests a contralateral front leg contribution to rhythmic neural activity

A stride consists of sequential left and right steps typically coordinated in antiphase (DeAngelis et al., 2019; Mendes et al., 2013; Wosnitza et al., 2013). When the fly walks straight, the left-right pair contributes equally to acceleration, thus creating two peaks in Vf during the stride cycle (Figure S4A). In contrast, HS-cell activity displayed only a single peak per stride (Figure S4A), suggesting that one leg predominantly modulates their activity. To evaluate which leg (i.e., left versus right) is the major contributor, we focused on front legs since they modulated HS cells stronger than the middle legs (Figures S4B and S4C). When the fly drifted from a straight course, the relation between the stride cycle and Vf was single peaked. The peak of Vf occurred at the stance phase of the side dominating the acceleration and driving angular drifts (Figure S4D) and coincided with the peak of $Vm_{|5\ Hz|}$ only when the contralateral front leg dominated the acceleration (e.g., during contraversive rotations) (Figures S4D–S4F). Thus, the oscillations in HS cells seemed to reflect contralateral leg movement rather than fluctuations in Vf (Figure 2).

Given the phase relation between $Vm_{|5\ Hz|}$ and the left front leg's stride cycle (Figure 3F), HS cells may be hyperpolarized during the stance phase of the contralateral leg (Model 1; Figure S4G, left) or depolarized during the stance phase of the ipsilateral leg

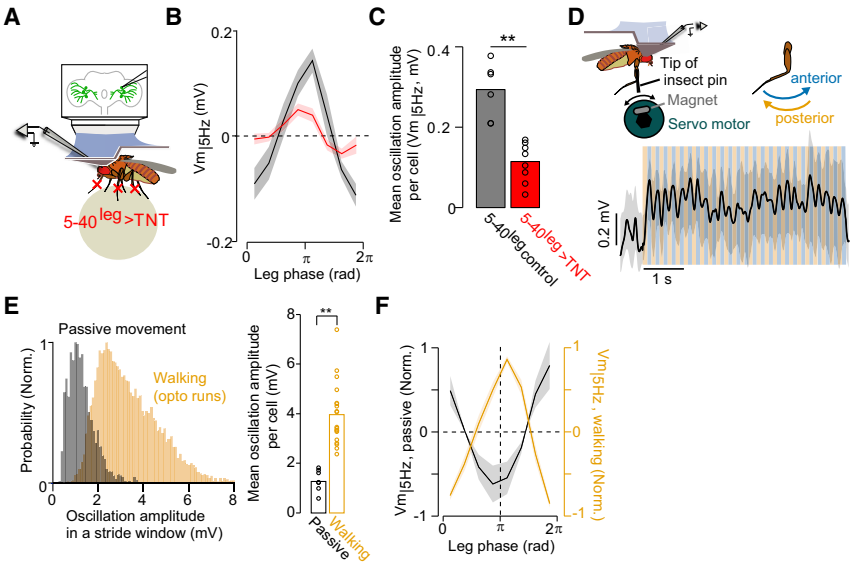

Figure 4. The stride-coupled modulation in HS cells depends on leg mechanosensory signals

(A) Schematic of the experimental configuration.

(B) $Vm_{|5\ Hz}$ as a function of the stride cycle of the left front leg (grand mean ± SEM). Red, 5-40^{leg} > TNT flies (n = 8 fly cell pairs); black, controls (n = 6 fly cell pairs).

(C) Mean amplitude of oscillations of $Vm_{|5\ Hz}$ (**p = 0.00067, the rank-sum test).

(D) Top, schematic of the experimental configuration. Bottom, time series of Vm (mean ± SD, n = 10 trials) during passive leg motion along the anterior (blue)-posterior (orange) axis.

(E) Distribution of the magnitude of oscillations in Vm during walking (orange, same as in Figure 3C) and passive leg motion (gray, 1,920 fictive strides from 8 flies). Right, mean amplitude of oscillations per cell during walking (3.95 ± 0.29 mV) and passive leg motion (1.27 ± 0.15 mV) ($p < 10^{-4}$, $Z = 4$, the rank-sum test).

(F) $Vm_{|5\ Hz}$ as a function of the stride (orange)/passive motion (black) cycle. Curves were normalized per cell. See also Figure S5.

(Model 2; Figure S4G, right). Model 1 predicts that oscillations in HS cells and Vf should correlate strongly during left drifts, whereas the converse is predicted by Model 2. By design, simulations showed that either model replicated the observed phase relation between the stride cycle and $Vm_{|5\ Hz}$ (Figure S4I; STAR Methods). However, Model 1 and not Model 2 replicated the relation between Vf and $Vm_{|5\ Hz}$ under angular drift as observed in the data (Figures S4J and S4K). These results support a model in which a unilateral leg-related sensorimotor network configures activity in the contralateral HS cells to respond rapidly.

Rhythmic activity in HS cells depends on leg sensorimotor circuits

To directly examine if neural signals from leg sensorimotor circuits contribute to the stride-coupled activity in HS cells, we perturbed chemical synaptic transmission in a large population of leg mechanosensory neurons via selective expression of tetanus toxin (Mendes et al., 2013) (Figure 4A). Recordings from HS cells in experimental flies during spontaneous high-speed walking (>5 mm/s) showed that the stride-coupled dynamics were largely degraded, although not fully abolished (Figures 4B and 4C). Perturbations in signal transmission within leg sensorimotor circuits can lead to deficits in leg coordination that might indirectly perturb oscillations in $Vm_{|5\ Hz}$ (Fujiwara et al., 2017; Mendes et al., 2013). Therefore, we analyzed neural activity in walking segments with leg trajectories indistinguishable between experimental and control flies, and in which oscillations in $Vm_{|5\ Hz}$ are readily observed in control flies (Figure S5A). In these selected walking bouts, the amplitude of the leg trajectories was larger in experimental versus control flies; however, the relation between the leg trajectories and $Vm_{|5\ Hz}$ was less organized, and the stride-coupled oscillations were still smaller in experimental flies than those observed in control flies (Figures S5A–S5C). Moreover, we reasoned that if the stride-coupled signals originate from internal circuits, the oscillations in $Vm_{|5\ Hz}$ should be relatively independent of leg kinematics. However, the strength of the rhythmic activity in HS cells at stride-cycle frequencies, as reported by the power spectral density, was smaller in experimental versus control flies (Figures S5D and S5E). These observations, together with the findings in opto-run flies (Figure S3), favor the idea that the oscillations in $Vm_{|5\ Hz}$ are at least partially dependent on the activity of leg mechanosensory neurons.

To determine whether activity in leg mechanosensory signals is sufficient to induce oscillations in HS cells, we passively moved the front leg along the anterior-posterior axis with a magnetic system (Mamiya et al., 2018) (Figure 4D). Despite the unnatural leg trajectories, these passive movements produced periodic activity in HS cells (Figure 4D). However, the amplitude of the oscillation in $Vm_{|5\ Hz}$ and the phase relation to the leg movement was a fraction and opposite to that observed during walking, respectively (Figures 3C, 4E, and 4F). These differences may arise from the movement of one rather than six legs, the activation of different sensory systems due to the lack of surface contact or of additional internal gating signals between standing and walking within VNC networks (Bässler and Büschges, 1998; O'Sullivan et al., 2018; Tuthill and Azim, 2018). Nevertheless, these findings are consistent with the idea that leg mechanosensory activity ascends to visual circuits and contributes to driving stride-coupled modulations in the activity of HS cells.

The stride-coupled modulation tunes neural activity correlated with rapid steering

We postulated that the stride-coupled oscillations may provide a timing signal that tunes HS activity at a precise moment within the stride cycle for steering adjustments (Figure 5A). If this were the case, there should be a positive correlation between activity in HS cells within a stride and a decrease in angular drift in the following stride. To test this idea, we examined walking segments drifting in the preferred, contraversive direction of HS cells (Figure 1C; Fujiwara et al., 2017) and when the peak of Vf coincides with the peak of $Vm_{|5\ Hz}$ within the stride cycle (Figures S4D and S4F). This allowed us to examine neural activity within a time

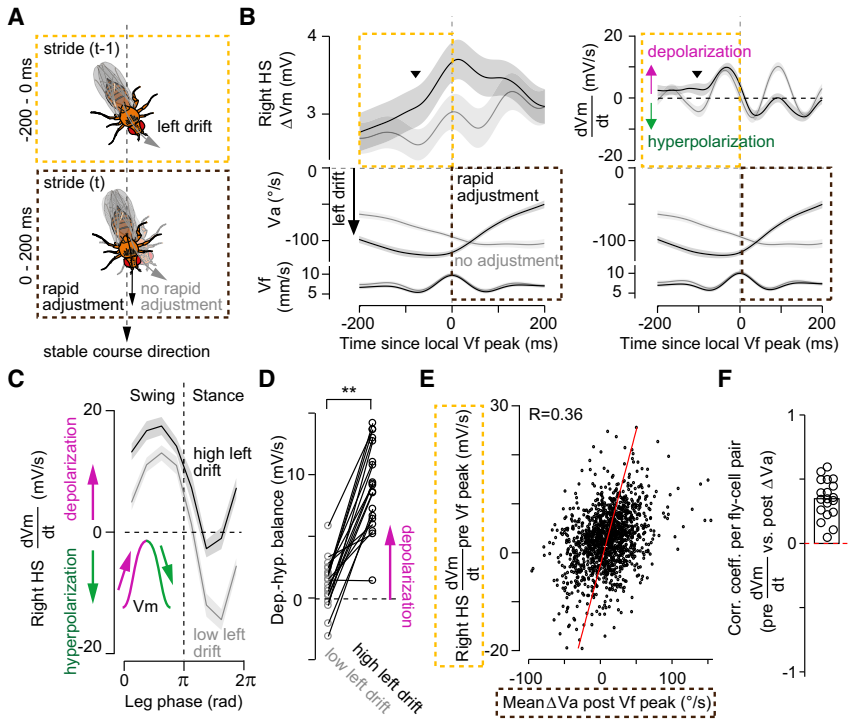

Figure 5. Imbalanced depolarization-hyperpolarization in HS cells within a stride correlates with rapid steering adjustments

(A) Schematic with time windows used for analysis.

(B) ΔVm (left), or its temporal derivative dVm/dt (right), Va, and Vf triggered at the local Vf peak in walking segments drifting leftwards (Va < −50°/s, grand mean ± SEM, n = 19 fly cell pairs). Traces were separated based on drift adjustment after the peak in Vf. Arrowheads highlights an overall increase in ΔVm for segments with rapid adjustments (black trace).

(C) dVm/dt as a function of the stride cycle of the left front leg during low (−50 < Va < 0°/s) or high (−200 < Va < −150°/s) drift.

(D) Depolarization-hyperpolarization balance across strides during low or high drift (p = 0.00016, Z = −3.78, n = 19 fly cell pairs, signed-rank test).

(E) Mean dVm/dt before peak Vf (−200:0 ms window, with peak Vf at 0, see A) as a function of the mean drift attenuation after peak Vf (0–200-ms window) for every segment (n = 1,378 segments from 19 fly cell pairs). The linear regression fit is indicated.

(F) Correlation between dVm/dt before peak Vf and drift attenuation after Vf per cell. The correlation was consistently positive (p = 0.00013, Z = 3.82, n = 19 fly cell pairs, the signed-rank test).

See also Figure S6.

window of 400 ms, on average 2 strides in opto-runs (Figures 3B and S2D), centered at the local peak of the fast fluctuations of Vf. To investigate the temporal relation between the neural activity in one stride and angular drifts (or Va) in the following stride, we separated the time course of the Vm and Va based on the decrease in magnitude of Va within the 200 ms following the local peak of Vf ("rapid adjustments") and then examined the corresponding Vm within the 200 ms preceding Vf peak (Figures 5A and 5B). On average, HS cells were more depolarized at about 100 ms before the local peak of Vf in segments with versus without rapid adjustments (Figure 5B, left). The increased neural activity was likely due to the observed reduction in hyperpolarization, as revealed by the temporal derivative of HS cells' Vm (dVm/dt) (Figure 5B, right), suggesting that a depolarization-hyperpolarization balance within a stride cycle may be rapidly tuned according to the fly's specific walking state. Thus, we next analyzed the neuron's dVm/dt triggered by the front leg's stride cycle and contingent on the ongoing state of Va. For walking segments with low drift (−50 < Va < 0°/s), HS cells were depolarized during the swing and hyperpolarized during the stance phases (Figure 5C), with balanced depolarization-hyperpolarization over the stride cycle (Figure 5D). In contrast, in walking segments with a higher drift (−200 < Va < −150°/s), the depolarization phase was longer and the hyperpolarization phase shorter over the stride cycle, resulting in an overall shift to depolarization (Figures 5C and 5D). Thus, the interaction between the ongoing state of Va and the stride-coupled modulation leads to a rapid, non-linear amplification in Vm (Figure 5B) that was based on a reduced hyperpolarization during stance (Figure S6A). These findings show that the activity in HS cells is fine-tuned on a stride timescale.

If this rapid tuning in neural activity contributed to steering within a stride, then we should observe a correlation between activity in HS cells and rapid adjustments in the following stride when evaluated across every 400 ms walking segment centered at the peak of Vf ("event-based correlation"). Indeed, the preceding dVm/dt was moderately but significantly correlated with the rapid adjustments on this event-based analysis (Figure 5E, n = 1,378 segments from 19 fly cell pairs), which was consistent across the recorded cells (Figure 5F). The correlation was independent of Va preceding the peak of Vf (Figures S6B–S6F), known to modulate the Vm at longer timescales (Fujiwara et al., 2017). Altogether, these findings suggest that stride-coupled modulations provide a timing signal to rapidly tune the activity in HS cells that may regulate rapid steering adjustments.

A rapid depolarization in HS cells leads to steering in a stride context-dependent manner

If the oscillations in $Vm_{|5\ Hz}$ contributed to rapid adjustments, perturbing them should degrade the event-based correlation. We tested this idea in flies with compromised synaptic activity in leg mechanosensory neurons, in which we found degraded stride-coupled oscillations in $Vm_{|5\ Hz}$ and in dVm/dt, even at relatively high Va (Figures 4B, 4C, and 6A). Consistent with a timing function, we found that in experimental flies with reduced stride-coupled oscillations, the dVm/dt did not correlate with rapid steering adjustments (Figures 6B and 6C). That is, activity in HS cells was uncoupled from rapid steering adjustments, suggesting that the oscillations in $Vm_{|5\ Hz}$ entrain their activity for stride-based steering.

To establish a direct effect of the activity of HS cells on steering at stride timescale, we performed brief optogenetic activation by expressing the excitatory opsin ReaChR specifically in HS cells in blind flies, and then stimulating them with light delivered only to the right brain hemisphere and conditioned to

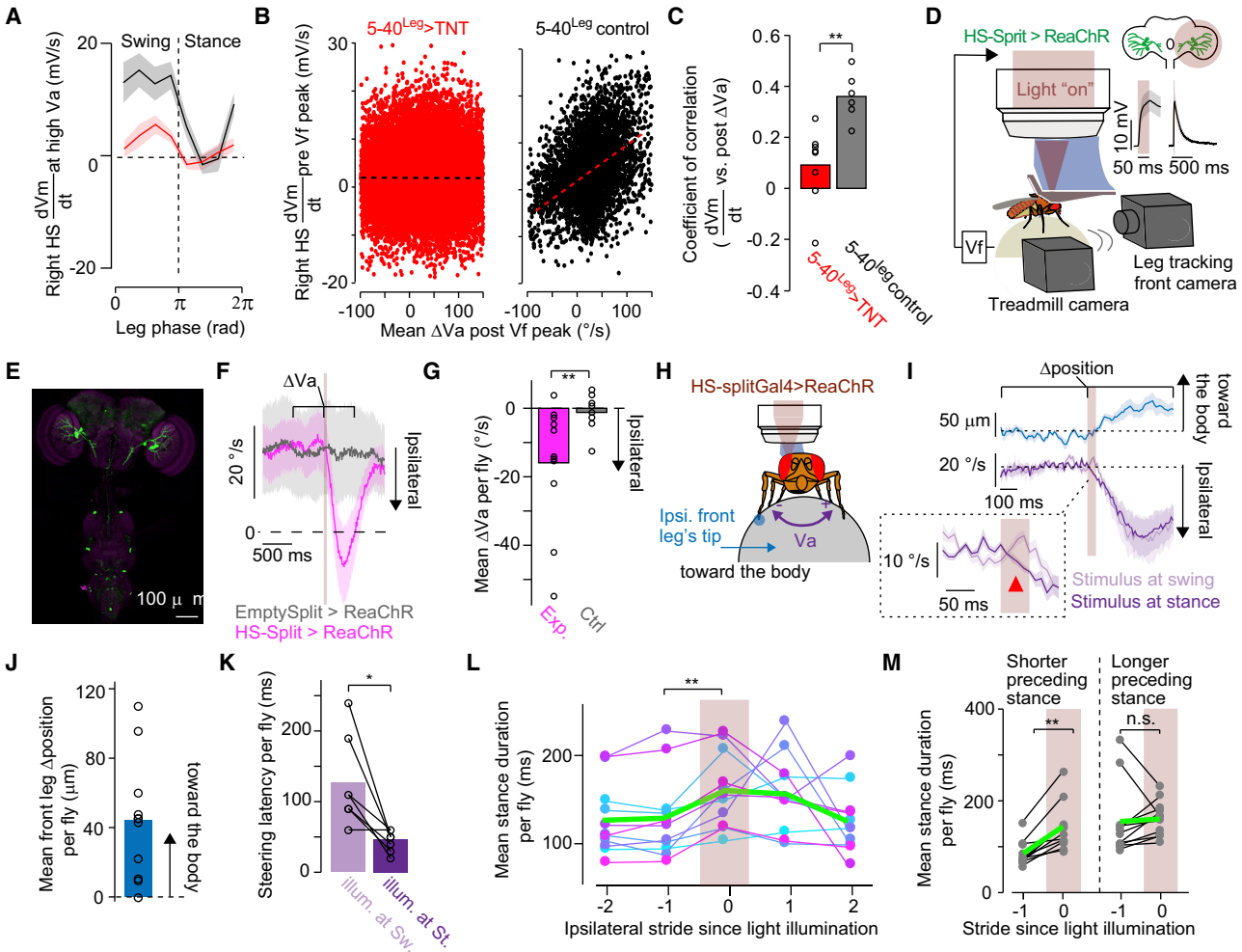

Figure 6. A rapid depolarization in HS cells leads to steering in a stride-dependent manner

(A) dVm/dt (right HS cells) in segments drifting leftwards ($-200 < Va < -150$°/s) as a function of the stride cycle (left front leg) in 5-40^{Leg} > TNT (red, grand mean ± SEM, n = 8 fly cell pairs) or control (black, n = 6 fly cell pairs) flies.

(B) Mean dVm/dt before peak Vf as a function of the drift attenuation after peak Vf (see Figure 5) per walking segment (5-40^{Leg} > TNT, red: n = 18,319 segments; control, black: n = 3,065 segments). Linear regression fits are indicated (5-40^{Leg} > TNT: R = −0.01, p = 0.41; control: R = 0.38, p < 10^{-16}, Student's t test).

(C) Analysis in (B) was performed per fly (p = 0.0013, the rank-sum test).

(D) Schematic of the experimental configuration. The inlet shows ReaChR-expressing HS cells' response to light (red shades) at different timescales (n = 9 cells).

(E) Confocal image of the split-HS line expressing ReaChR.

(F) Va traces in experimental (magenta, n = 11 flies) and control (gray, n = 8 flies) flies triggered at light stimulation.

(G) Mean change in Va (ΔVa) per fly upon light stimulation (p = 0.0091, the rank-sum test).

(H) Schematic of the experimental configuration.

(I) The leg's horizontal position (n = 11 flies) and the fly's Va (baseline subtracted per fly, n = 7 flies), triggered at light stimulation (red shade). Va traces are separated by the stride-cycle phase of the leg at stimulation, either in swing (light purple) or stance (dark purple). The inlet highlights the onset steering response, with the red arrowhead indicating the offset between the traces.

(J) Mean shift in leg position (Δposition) per fly (p = 0.0020, n = 11 flies, the rank-sum test).

(K) Steering onset latency for stimulation at swing (light purple) or stance (dark purple, p = 0.031, n = 7 flies, the signed-rank test).

(L) Mean stance duration of five consecutive strides around light stimulation (strides preceding versus at stimulation: p = 0.0020, n = 11 flies, the signed-rank test). Colored lines show individual fly data and green indicate the grand mean.

(M) Mean stance duration of strides preceding versus at light delivery, in strides with shorter (p = 0.0010, left) or longer (p = 0.32, right) preceding stance duration. n = 11 flies, signed-rank test.

See also Video S2.

high-speed walking (Figures 6D and 6E). We chose a duration of stimulation on the timescale of a leg swing (50 ms) when HS cells are depolarized during the contralateral leg's stride cycle (Figure 5C). The brief stimulation was effective in depolarizing HS cells (Figure 6D inlet left, latency = 4.9 ± 0.8 ms, n = 9 cells, mean ± SEM). Although the depolarization lasted longer than

the stimulus (Figure 6D inlet right, falling time constant = 247 ± 46 ms), the effect on behavior was observed already within the stimulation window (see below). This brief stimulation of HS cells promoted ipsilateral steering in experimental but not control flies (Figures 6F and 6G), consistent with previous studies looking at the effect of HS cells' activity on behavior at much longer timescales (Busch et al., 2018; Fujiwara et al., 2017). Thus, the activity in HS cells modulates leg circuits rapidly to contribute to directed steering adjustments.

To monitor how HS cells induce rapid ipsilateral steering, we tracked the front legs (Figures 6D and 6H) because they are the main contributors to steering during forward runs (Cruz et al., 2021). Upon neural activation, the ipsilateral front leg moved toward the body consistently (Figures 6I and 6J; Video S2). Because a walking fly generates reactive forces during the stance phase of the stride cycle, we speculated that HS cells may contribute to steering by acting on the ipsilateral front leg during the stance phase. Consistent with this hypothesis, we found that the latency of the steering response was shorter when the light was delivered at the stance versus swing phase of the ipsilateral leg (Figures 6I and 6K). Moreover, the brief activation of HS cells extended the stance phase (Figure 6L; Video S2). Interestingly, this effect was observed when the preceding stride had a short stance duration (Figure 6M). Altogether, these findings show that the timing of the depolarization of HS cells within a stride appears precisely aligned to modulate the ipsilateral front leg during stance for rapid steering, especially when the fly walks with strides of short duration. That is, HS cells can drive rapid steering adjustments in part via the regulation of the ipsilateral front leg stance duration. These findings, together with the contribution of synaptic activity from the leg mechanosensory neurons to the stride-coupled oscillations in $Vm_{|5\ Hz}$, strongly suggest that ascending pathways from the VNC may provide the timing signal to HS cells.

LAL-PS-ANs$_{contra}$ contribute to the stride-coupled modulation in HS cells

Based on the suggested contralateral connectivity (Figure S4), we sought to identify candidate ANs contributing to the stride-coupled modulation. HS cell axons terminate within the PS, richly innervated by ANs (Strausfeld, 1976). Assuming that HS cells receive ascending inputs at the PS (i.e., at their axons), we searched for candidate ANs innervating the PS using an electron microscopy (EM) dataset (Scheffer et al., 2020). We then applied computational tools to identify the EM-traced skeleton in light microscopy images from transgenic lines (Meissner et al., 2020). Following this systematic approach, we identified a pair of previously undescribed ANs that innervate the front and middle leg neuropil, cross the commissure in the VNC, and project to the contralateral PS and a higher premotor region, LAL (Figures 7A and S7A–S7D). We defined these ANs as "LAL-PS-AN$_{contra}$." Despite their convergent and overlapping projections at PS, LAL-PS-AN$_{contra}$ does not provide direct chemical synapses onto HS cells (Figures S7D and S7E). In fact, LAL-PS-AN$_{contra}$ is one to three synapses away from each HS cell (Figure S7E). Nevertheless, optogenetic activation of LAL-PS-AN$_{contra}$ induced a robust response in HS cells (Figure 7B). Although silencing the activity of only these two AN cells did not affect the fly's overall walking (experimental n = 13 versus GAL4 control n = 12 versus UAS control n = 14 flies; absolute Va = 53.0 ± 2.7 versus 46.2 ± 3.4 versus 54.0 ± 4.7°/s, p = 0.11, $Z = 1.60$ or p = 0.87, $Z = 0.17$ against GAL4 or UAS control; Vf = 3.0 ± 0.3 versus 3.3 ± 0.3 versus 2.7 ± 0.2 mm/s, p = 0.43, $Z = -0.79$ or p = 0.54, $Z = 0.60$ against GAL4 or UAS control, mean ± SEM, the rank-sum test), the manipulation significantly decreased the magnitude of the stride-coupled oscillations in $Vm_{|5\ Hz}$ (Figures 7C and 7D). These findings support the contribution of LAL-PS-ANs$_{contra}$ to the stride-coupled modulation and demonstrate that, at least in part, this timing signal arrives at PS via ascending pathways from the VNC.

To evaluate the response properties of LAL-PS-AN$_{contra}$, we performed two-photon calcium imaging at their axons in walking flies (Figure 7E). LAL-PS-AN$_{contra}$ activity was positively correlated with Vf and relatively insensitive to Va (Figures 7E–7G). Moreover, the activity in this class of ANs was greater in walking than grooming (Figures 7H and 7I). Altogether, these findings reveal a pathway that informs of the state of Vf and not of Va (motor context) and that connects stride-coupled signals from the VNC to oscillatory activity in brain visuomotor circuits.

The stance duration over several strides provides an internal motor context

Because LAL-PS-AN$_{contra}$ activity is correlated with Vf, and silencing their activity decreased the oscillations in $Vm_{|5\ Hz}$, the stride-coupled signals could also contribute to the representation of Vf at longer timescales (Figure 1). Our data show that the stance phase of the contralateral front leg provides a hyperpolarizing drive to HS cells (Figures 3, 5, and S4). Stance duration is inversely correlated with Vf in freely walking animals (DeAngelis et al., 2019; Mendes et al., 2013; Szczecinski et al., 2018), as well as in our head-fixed flies walking on a ball (Figures 8A and S8A). Therefore, we reasoned that the stance duration over sequential strides could drive a cumulative signal representing the state of Vf over seconds (motor context). Consistent with this idea, we found that HS cells were more hyperpolarized at the end relative to the beginning of a stride with a long but not short stance duration (Figures 8B and 8D). If the fly executes sequential strides of similar stance duration, then the modulatory effect per stride would build up a slow hyperpolarization in HS cell activity. Indeed, this was the case for walking at slow speed, whereas we observed a depolarizing trend at high-speed walking, i.e., with strides with short stance duration (Figures 8C, 8D, S8B, and S8C). Consistent with the proposed underlying connectivity structure (Figures S4 and 7), this slow modulation was observed when $Vm_{|5\ Hz}$ was aligned to the contralateral and not the ipsilateral front leg phase (Figures S8D–S8G).

If the emergence of the information about motor context in HS cells also originates from the stride-coupled signals (Figure 5), then perturbing synaptic activity in leg mechanosensory neurons, which contribute to the oscillations in $Vm_{|5\ Hz}$ (Figures 4B and 4C), should decrease the stance-dependent hyperpolarization over sequential similar strides. Evaluating the activity of HS cells in experimental flies showed that the stance-related hyperpolarization was significantly decreased (Figures 8E and 8F). Consistent with the idea that the stance-based hyperpolarization mechanism configures a motor context modulation in HS cells (Figure 1C), the sensitivity to Vf in HS cells was also

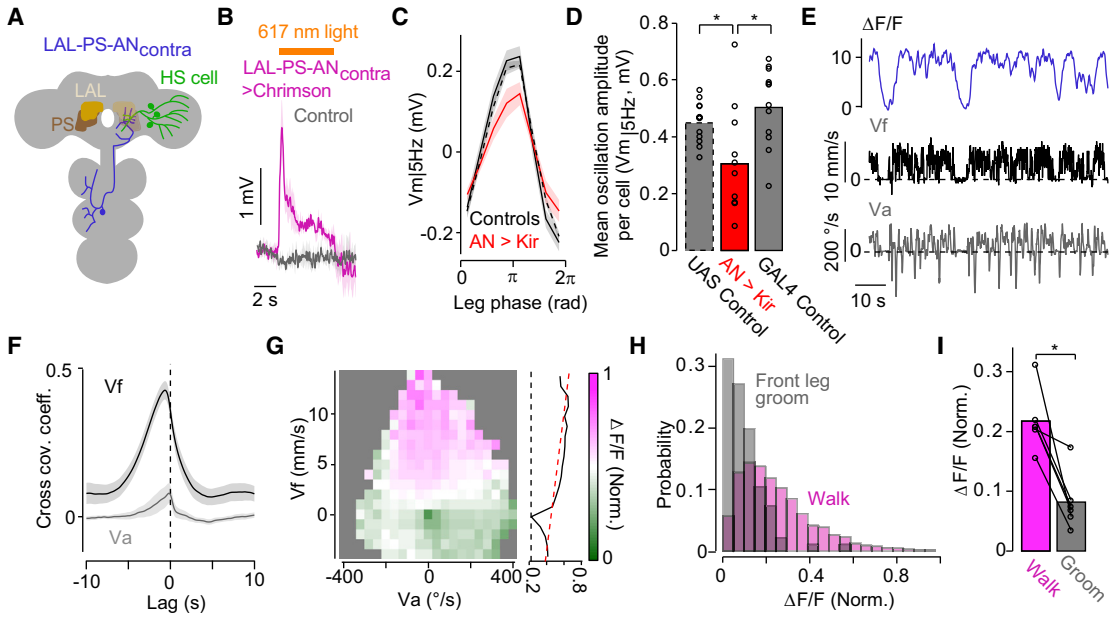

Figure 7. Vf-sensitive ascending neurons (ANs) contribute to the stride-coupled modulation

(A) Schematic of the anatomy of the identified ANs.

(B) HS cells' activity upon optogenetic activation of LAL-PS-AN$_{contra}$ (orange bar) in experimental (magenta, grand mean ± SEM, n = 5 cells) or control (gray, n = 3 cells) flies.

(C) Vm$_{|5\ Hz}$ as a function of the stride cycle (left front leg) in AN-silenced (red, n = 11 fly cell pairs), GAL4 (solid black, n = 12 fly cell pairs), and UAS (dashed black, n = 14 fly cell pairs) control flies.

(D) Mean Vm$_{|5\ Hz}$ oscillation amplitude in experimental (red), GAL4 (solid black, p = 0.029, $Z = -2.18$, signed-rank test) and UAS (dashed black, p = 0.040, $Z = -2.05$, the signed-rank test) controls.

(E) Example traces of the left LAL-PS-AN$_{contra}$ (calcium signal, ΔF/F), Vf, and Va.

(F) The cross-covariance coefficient between ΔF/F and Vf or Va (n = 7 fly cell pairs).

(G) ΔF/F (normalized per fly and pooled across 7 flies) as a function of Va and Vf. Right, the Vf tuning (mean ΔF/F over Va) plotted with a linear fit.

(H) Probability distributions of the magnitude of ΔF/F in walking (magenta, 2,909 events from 6 flies) versus front leg grooming (gray, 96 events).

(I) Mean ΔF/F in walking versus grooming per fly (p = 0.031, n = 6 fly cell pairs, the signed-rank test).

See also Figure S7.

significantly decreased (Figure 8G). Altogether, these findings demonstrate that the stance duration over sequential strides configures a motor context signal reflecting the state of Vf over timescales longer than a stride, thereby explaining how HS cells can be flexibly recruited to contribute to online rapid steering adjustments.

DISCUSSION

A critical component of adaptive behavior is the provision of continuous feedback on the state of the body, which defines a motor context that flexibly recruits neural activity given the task at play. How this feedback originates and orchestrates neural activity have been poorly understood. Here, we reveal that a component of the internal motor context originates in leg-related circuits and rapidly recruits a visuomotor circuit for online heading adjustments specifically during fast walking (Figure 8H). Activity in HS cells is rhythmically fine-tuned by walking strides such that the contralateral leg's swing and stance phases depolarize and hyperpolarize the neurons, respectively (Figures 3 and 5). During contraversive angular drifts, HS cell activity is amplified at a proper time within a stride to extend the ipsilateral leg's stance phase in the next stride, thereby contributing to a fast corrective steering maneuver (Figures 5, 6, and 8I) (Cruz et al., 2021; Isakov et al., 2016). Notably, strides with long stance duration can only barely be further extended by HS cells (Figure 6). Thus, rapid correction by HS cells only occurs in the context of strides with short stance duration. Moreover, at longer timescales, activity in HS cells steadily goes up or down depending on the stance duration of the sequential strides (Figure 8). Because the stance but not the swing duration changes with walking speed (Mendes et al., 2013; Wosnitza et al., 2013), the stance-dependent tuning of the activity in HS cells and their effect on behavior defines a motor context that faithfully reflects the state of Vf conveyed by ANs (Figures 7 and 8I). Given the dynamical nature of locomotion, in which errors must be quickly corrected to avoid their fast amplification (Bernstein, 1967), a single mechanism based on the stance, operating both at single and multiple stride timescales, elegantly accomplishes rapid steering adjustments via the flexible recruitment of visual circuits. Altogether, our work reveals a mechanistic link between a movement parameter correlated with walking speed—stance duration—a speed representation in the central brain, and their effect on neural activity and behavior.

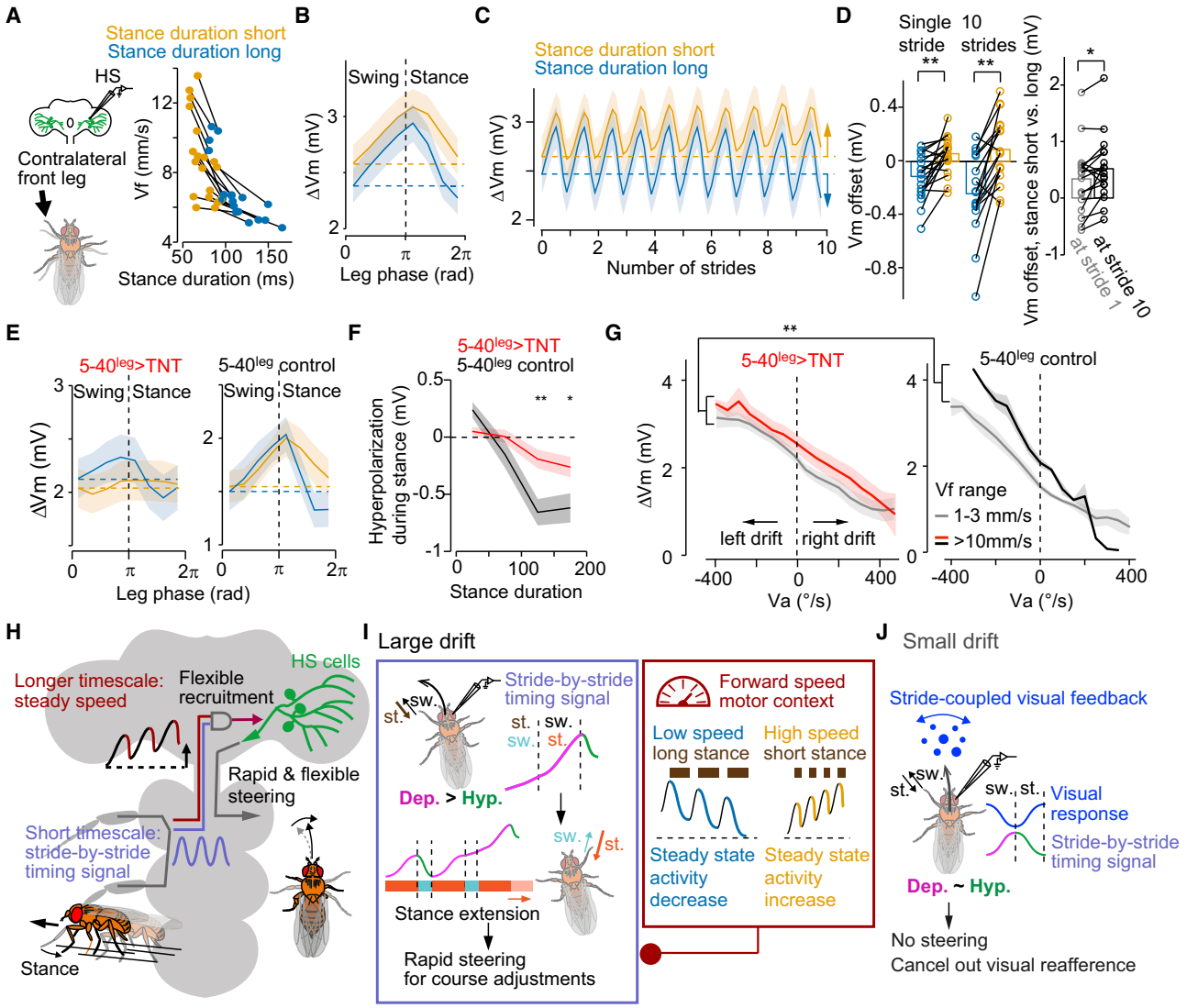

Figure 8. The duration of the stance controls the hyperpolarization in HS cells at multiple timescales

(A) Left, schematic of the experimental configuration. Right, the relation between Vf and stance duration during head-fixed walking on the ball. Orange/blue: short/long stances (n = 19 fly cell pairs; lines connect the same individual). The fly walks faster with shorter stances (p = 0.000163, $Z = 3.82$, the signed-rank test).

(B) ΔVm (grand mean ± SEM, n = 19 fly cell pairs) as a function of the stride cycle for shorter (orange) and longer (blue) stances.

(C) Same as (B), but for 10 consecutive strides (n = 17 fly cell pairs).

(D) The difference between Vm at the beginning versus the end ("offset," dashed lines in B and C) of a single (left) or ten consecutive strides (middle). p = 0.00054, $Z = -3.46$, n = 19 fly cell pairs for a single stride; p = 0.00060, $Z = -3.43$, n = 17 fly cell pairs for ten strides. Right, the offset in Vm was compared between the end of stride 1 and 10. P = 0.019, $Z = -2.34$, n = 17 fly cell pairs, the signed-rank test.

(E) Same as (B) but for 5-40^{Leg} > TNT (n = 8 fly cell pairs) and control (n = 6 fly cell pairs) flies.

(F) The hyperpolarization of HS cells during stance as a function of stance duration (5-40^{Leg} > TNT, red, n = 8 fly cell pairs; control, black, n = 6 fly cell pairs). *p < 0.05; **p < 0.01, the rank-sum test.

(G) ΔVm as a function of Va during low and high Vf in 5-40^{Leg} > TNT (n = 8 fly cell pairs) and control (n = 5 fly cell pairs) flies. Vf-dependent Vm offset in 5-40^{Leg} > TNT flies was smaller than in control flies (**p = 0, bootstrapping, see also Figure 1).

(H–J) Summary of the findings (H) and the proposed function for the stride-coupled modulation during fast and drifting walking (I) and during fast, straight walking (J) in HS cells.

See also Figure S8.

Stride-coupled modulation of central brain circuits for movement correction

The stride-coupled modulations in HS cells operate independently of vision and do not fit the conventional notion of an efference copy, a motor-related signal that cancels out sensory reafference (Crapse and Sommer, 2008). Although efference-copy-like signals have been described in HS cells during rapid head and body turns in flight (Kim et al., 2015, 2017), our results

during fast walking are rather in line with a multimodal estimate of self-rotations for a steering maneuver that operates at a much faster timescale than previously anticipated (Figures 2 and 5) (Fujiwara et al., 2017). However, when the fly walks with no angular drift, the stride-coupled modulations in HS cells may effectively act similar to the efference-copy signals to maintain straight walking. During the stance phase, reaction forces induce the body to swivel toward the leg in stance, potentially producing visual motion signals that would stimulate the contralateral HS cells (inevitable self-stimulation). Thus, the hyperpolarizing phase in HS cells induced by the contralateral leg's stance may function as a suppressive signal alike those found in vertebrates to prevent HS excitation at an improper timing (Figure 8I) (França de Barros et al., 2022; Straka et al., 2018). Alternatively, because HS cells directly connect to neck motor neurons controlling head movements (Milde et al., 1987), the rapid depolarization of right HS cells during the contralateral front leg's swing phase might promote an anticipatory head rotation that compensates the upcoming body swivel thereby stabilizing gaze (Cruz et al., 2021). Further characterization on the temporal relationship between the head, body, and leg movements will be required to precisely evaluate visual self-stimulation on a stride timescale during walking.

Neural representation of a motor context

Our finding of stride-related signals in HS cells provides important insights into the source and function of movement-related signals in brain circuits, and more generally, into the mechanisms of motor context modulation by the activity of ANs from the VNC. Over the last decade, a considerable amount of work in rodents and insects has revealed prominent modulations in the activity of visual circuits during walking (Busse et al., 2017; Chiappe et al., 2010; McGinley et al., 2015; Niell and Stryker, 2010; Parker et al., 2020). Neural representations of Vf that can be linked to an animal's vigor to achieve a goal (Dudman and Krakauer, 2016), have been widely found in rodents (Busse et al., 2017; Carvalho et al., 2020; Fobbs et al., 2020; Kropff et al., 2015; Lu et al., 2022; Saleem et al., 2013; Wirtshafter and Wilson, 2019), insects (Fujiwara et al., 2017; Martin et al., 2015), worms (Kato et al., 2015; Li et al., 2014), and fish (Vinepinsky et al., 2020). The origin of these speed-related signals, however, has remained poorly understood. Here, we describe that the same source that drives stride-coupled oscillations in visual neurons configures a slower modulation that contributes to the representation of Vf in a visuomotor circuit. Given that in many brain regions of the mammalian brain the presence of stride-coupled dynamics is well established (Orlovsky et al., 1999), the origin and mechanisms for the Vf representation and modulation of neural activity reported here in *Drosophila* may likely be present in other organisms, including mammals.

Outlook

Speed-related signals are critical for vector computation in path integration (Kropff et al., 2015; McNaughton et al., 2006) and coordinate transformations (Lu et al., 2022; Lyu et al., 2022). A mechanism integrating the stride-coupled activity over several strides (Figure 8) could subserve as a step counter for path integration (Stone et al., 2017; Wittlinger et al., 2006). Therefore, we speculate that similar stride-coupled signals may be transmitted to higher-order brain circuits involved in navigation and motor control. This hypothesis is supported by the finding that LAL-PS-ANs$_{contra}$ project to the PS and LAL (Figures 7 and S7), two major brain areas implicated in motor control. Future research will reveal how our findings can be generalized and further extended to other circuits in flies and corresponding systems in other animal species.

STAR★METHODS

Detailed methods are provided in the online version of this paper and include the following:

- KEY RESOURCES TABLE
- RESOURCE AVAILABILITY
  - Lead contact
  - Materials availability
  - Data and code availability
- EXPERIMENTAL MODEL AND SUBJECT DETAILS
- METHOD DETAILS
  - Detailed fly genotypes used by figures
  - Electrophysiological and calcium recordings
  - Chemogenetic silencing of HS cells
  - Optogenetic activation of BPNs or HS cells
  - HS-cell recording under visual feedback
  - HS-cell recording with external leg movement
  - Immunostaining
- QUANTIFICATION AND STATISTICAL ANALYSIS
  - Processing of physiology and behavior data
  - Leg tracking
  - Simulation
  - Ball stop experiment
  - External leg movement experiment
  - Calcium imaging
  - Anatomy
  - Statistics

SUPPLEMENTAL INFORMATION

Supplemental information can be found online at https://doi.org/10.1016/j.neuron.2022.04.008.

ACKNOWLEDGMENTS

We thank Nélia Varela for stock construction and maintenance and immunostaining; Sebastián Malagon for the analysis with DeepEthogram; and Ibrahim Taştekin, Gregory Jefferis, and Alexander Bates for technical support for image registration. We are grateful for helpful discussions and comments on the manuscript by Maximilian Jösch and members of the Chiappe laboratory. We thank S. Bidaye, G. Card, M. Dickinson, C. Mendes, V. Ruta, and M. Silies for fly stocks. This work was supported by the Champalimaud Foundation and the research infrastructure Congento, LISBOA-01-0145-FEDER-022170, co-financed by Fundação para a Ciência e Tecnologia (Portugal) and Lisboa 2020, under the PORTUGAL 2020 Agreement (European Regional Development Fund). This work was also supported by the Japanese Society for the Promotion of Science (JSPS) Overseas Research Fellowship 20170687 (T.F.), by the Marie Curie Career Integration Grant PCIG13-GA-2013-618854, and by the European Research Council Starting Grant ERC-2017-STG-759782 (M.E.C.).

AUTHOR CONTRIBUTIONS

Conceptualization, T.F. and M.E.C.; methodology, T.F.; investigation, T.F. and M.B.; formal analysis, T.F., M.B., and M.E.C.; supervision M.E.C.; writing, T.F. and M.E.C.

DECLARATION OF INTERESTS

The authors declare no competing interests.

INCLUSION AND DIVERSITY

While citing references scientifically relevant for this study, we worked to promote gender balance in our reference list as much as possible.

Received: September 13, 2021
Revised: January 31, 2022
Accepted: April 8, 2022
Published: May 6, 2022

REFERENCES

Augustine, V., Lee, S., and Oka, Y. (2020). Neural control and modulation of thirst, sodium appetite, and hunger. Cell *180*, 25–32.

Bargmann, C.I. (2012). Beyond the connectome: how neuromodulators shape neural circuits. BioEssays *34*, 458–465.

Bässler, U., and Büschges, A. (1998). Pattern generation for stick insect walking movements—multisensory control of a locomotor program. Brain Res. Brain Res. Rev. *27*, 65–88.

Bates, A.S., Manton, J.D., Jagannathan, S.R., Costa, M., Schlegel, P., Rohlfing, T., and Jefferis, G.S.X.E. (2020). The natverse, a versatile toolbox for combining and analysing neuroanatomical data. eLife *9*, 1–35.

Bernstein, N. (1967). The Coordination and Regulation of Movements (Pergamon Press).

Bidaye, S.S., Laturney, M., Chang, A.K., Liu, Y., Bockemühl, T., Büschges, A., and Scott, K. (2020). Two brain pathways initiate distinct forward walking programs in drosophila. Neuron *108*. 469.e8–485.e8.

Bloomquist, B.T., Shortridge, R.D., Schneuwly, S., Perdew, M., Montell, C., Steller, H., Rubin, G., and Pak, W.L. (1988). Isolation of a putative phospholipase C gene of *Drosophila, norpA*, and its role in phototransduction. Cell *54*, 723–733.

Bogovic, J.A., Otsuna, H., Heinrich, L., Ito, M., Jeter, J., Meissner, G., Nern, A., Colonell, J., Malkesman, O., Ito, K., and Saafeld, S. (2020). An unbiased template of the *Drosophila* brain and ventral nerve cord. PLoS One *15*, e0236495.

Bohnslav, J.P., Wimalasena, N.K., Clausing, K.J., Dai, Y.Y., Yarmolinsky, D.A., Cruz, T., Kashlan, A.D., Chiappe, M.E., Orefice, L.L., Woolf, C.J., et al. (2021). DeepEthogram, a machine learning pipeline for supervised behavior classification from raw pixels. eLife *10*, e63377.

Busch, C., Borst, A., and Mauss, A.S. (2018). Bi-directional control of walking behavior by horizontal optic flow sensors. Curr. Biol. *28*, 4037–4045.e5.

Busse, L., Cardin, J.A., Chiappe, M.E., Halassa, M.M., McGinley, M.J., Yamashita, T., and Saleem, A.B. (2017). Sensation during active behaviors. J. Neurosci. *37*, 10826–10834.

Carvalho, M.M., Tanke, N., Kropff, E., Witter, M.P., Moser, M.B., and Moser, E.I. (2020). A brainstem locomotor circuit drives the activity of speed cells in the medial entorhinal cortex. Cell Rep. *32*, 108123.

Chiappe, M.E., Seelig, J.D., Reiser, M.B., and Jayaraman, V. (2010). Walking modulates speed sensitivity in drosophila motion vision. Curr. Biol. *20*, 1470–1475.

Chun, C., Biswas, T., and Bhandawat, V. (2021). *Drosophila* uses a tripod gait across all walking speeds, and the geometry of the tripod is important for speed control. eLife *10*, 1–47.

Clements, J., Dolafi, T., Umayam, L., Neubarth, N.L., Berg, S., Scheffer, L.K., and Plaza, S.M. (2020). NeuPrint: analysis tools for EM connectomics. Preprint at bioRxiv. https://doi.org/10.1101/2020.01.16.909465.

Cohn, R., Morantte, I., and Ruta, V. (2015). Coordinated and compartmentalized neuromodulation shapes sensory processing in drosophila. Cell *163*, 1742–1755.

Crapse, T.B., and Sommer, M.A. (2008). Corollary discharge across the animal kingdom. Nat. Rev. Neurosci. *9*, 587–600.

Creamer, M.S., Mano, O., and Clark, D.A. (2018). Visual control of walking speed in drosophila. Neuron *100*. 1460.e6–1473.e6.

Cruz, T.L., Malagón Pérez, S., and Chiappe, M.E. (2021). Fast tuning of posture control by visual feedback underlies gaze stabilization in walking *Drosophila*. Curr. Biol. *31*. 4596.e5–4607.e5.

DeAngelis, B.D., Zavatone-Veth, J.A., and Clark, D.A. (2019). The manifold structure of limb coordination in walking *Drosophila*. eLife *8*, 1–34.

Dickinson, M.H., Farley, C.T., Full, R.J., Koehl, M.A., Kram, R., and Lehman, S. (2000). How animals move: an integrative view. Science *288*, 100–106.

Dudman, J.T., and Krakauer, J.W. (2016). The basal ganglia: from motor commands to the control of vigor. Curr. Opin. Neurobiol. *37*, 158–166.

Dürr, V. (2005). Context-dependent changes in strength and efficacy of leg coordination mechanisms. J. Exp. Biol. *208*, 2253–2267.

Fenk, L.M., Kim, A.J., and Maimon, G. (2021). Suppression of motion vision during course-changing, but not course-stabilizing, navigational turns. Curr. Biol. *31*, 4608–4619.

Fobbs, W.C., Bariselli, S., Licholai, J.A., Miyazaki, N.L., Matikainen-Ankney, B.A., Creed, M.C., and Kravitz, A.V. (2020). Continuous representations of speed by striatal medium spiny neurons. J. Neurosci. *40*, 1679–1688.

França de Barros, F., Bacqué-Cazenave, J., Taillebuis, C., Courtand, G., Manuel, M., Bras, H., Tagliabue, M., Combes, D., Lambert, F.M., and Beraneck, M. (2022). Conservation of locomotion-induced oculomotor activity through evolution in mammals. Curr. Biol. *32*. 453.e4–461.e4.

Fujiwara, T., Cruz, T.L., Bohnslav, J.P., and Chiappe, M.E. (2017). A faithful internal representation of walking movements in the *Drosophila* visual system. Nat. Neurosci. *20*, 72–81.

Giorgianni, M.W., and Mann, R.S. (2011). Establishment of medial fates along the proximodistal axis of the *Drosophila* leg through direct activation of dachshund by distalless. Dev. Cell *20*, 455–468.

Guizar-Sicairos, M., Thurman, S.T., and Fienup, J.R. (2008). Efficient subpixel image registration algorithms. Opt. Lett. *33*, 156–158.

Haikala, V., Joesch, M., Borst, A., and Mauss, A.S. (2013). Optogenetic control of fly optomotor responses. J. Neurosci. *33*, 13927–13934.

Hausen, K. (1984). The Lobula-complex of the fly: structure, function and significance in visual behavior. Photoreception and Vision in Invertebrates (New York and London: Plenum Press).

Hughes, C.L., and Thomas, J.B. (2007). A sensory feedback circuit coordinates muscle activity in Drosophila. Mol. Cell. Neurosci. *35*, 383–396.

Isakov, A., Buchanan, S.M., Sullivan, B., Ramachandran, A., Chapman, J.K.S., Lu, E.S., Mahadevan, L., and de Bivort, B. (2016). Recovery of locomotion after injury in *Drosophila melanogaster* depends on proprioception. J. Exp. Biol. *219*, 1760–1771.

Kabra, M., Robie, A.A., Rivera-Alba, M., Branson, S., and Branson, K. (2013). JAABA: interactive machine learning for automatic annotation of animal behavior. Nat. Methods *10*, 64–67.

Kato, S., Kaplan, H.S., Schrödel, T., Skora, S., Lindsay, T.H., Yemini, E., Lockery, S., and Zimmer, M. (2015). Global brain dynamics embed the motor command sequence of *Caenorhabditis elegans*. Cell *163*, 656–669.

Khan, A.G., and Hofer, S.B. (2018). Contextual signals in visual cortex. Curr. Opin. Neurobiol. *52*, 131–138.

Kim, A.J., Fenk, L.M., Lyu, C., and Maimon, G. (2017). Quantitative Predictions Orchestrate Visual Signaling in Drosophila. Cell *168*, 280–294.e12.

Kim, A.J., Fitzgerald, J.K., and Maimon, G. (2015). Cellular evidence for efference copy in *Drosophila* visuomotor processing. Nat. Neurosci. *18*, 1247–1255.

Kropff, E., Carmichael, J.E., Moser, M.-B., and Moser, E.I. (2015). Speed cells in the medial entorhinal cortex. Nature *523*, 419–424.

Li, Z., Liu, J., Zheng, M., and Xu, X.Z.S. (2014). Encoding of both analog- and digital-like behavioral outputs by one *C. elegans* interneuron. Cell *159*, 751–765.

Liu, W.W., and Wilson, R.I. (2013). Transient and specific inactivation of *Drosophila* neurons in vivo using a native ligand-gated ion channel. Curr. Biol. *23*, 1202–1208.

Lu, J., Behbahani, A.H., Hamburg, L., Westeinde, E.A., Dawson, P.M., Lyu, C., Maimon, G., Dickinson, M.H., Druckmann, S., and Wilson, R.I. (2022). Transforming representations of movement from body- to world-centric space. Nature *601*, 98–104.

Lyu, C., Abbott, L.F., and Maimon, G. (2022). Building an allocentric travelling direction signal via vector computation. Nature *601*, 92–97.

Maimon, G., Straw, A.D., and Dickinson, M.H. (2010). Active flight increases the gain of visual motion processing in *Drosophila*. Nat. Neurosci. *13*, 393–399.

Mamiya, A., Gurung, P., and Tuthill, J.C. (2018). Neural coding of leg proprioception in *Drosophila*. Neuron *100*. 636.e6–650.e6.

Maren, S., Phan, K.L., and Liberzon, I. (2013). The contextual brain: implications for fear conditioning, extinction and psychopathology. Nat. Rev. Neurosci. *14*, 417–428.

Martin, J.P., Guo, P., Mu, L., Harley, C.M., and Ritzmann, R.E. (2015). Central-complex control of movement in the freely walking cockroach. Curr. Biol. *25*, 2795–2803.

Mathis, A., Mamidanna, P., Cury, K.M., Abe, T., Murthy, V.N., Mathis, M.W., and Bethge, M. (2018). DeepLabCut: markerless pose estimation of user-defined body parts with deep learning. Nat. Neurosci. *21*, 1281–1289.

McGinley, M.J., Vinck, M., Reimer, J., Batista-Brito, R., Zagha, E., Cadwell, C.R., Tolias, A.S., Cardin, J.A., and McCormick, D.A. (2015). Waking state: rapid variations modulate neural and behavioral responses. Neuron *87*, 1143–1161.

McNaughton, B.L., Battaglia, F.P., Jensen, O., Moser, E.I., and Moser, M.-B. (2006). Path integration and the neural basis of the "cognitive map. Nat. Rev. Neurosci. *7*, 663–678.

Meissner, G.W., Dorman, Z., Nern, A., Forster, K., Jeter, J., Johnson, L., He, Y., Lee, K., Melton, B., Clements, J., et al. (2020). An image resource of subdivided *Drosophila* GAL4-driver expression patterns for neuron-level searches. Preprint at bioRxiv. https://doi.org/10.1101/2020.05.29.080473.

Mendes, C.S., Bartos, I., Akay, T., Márka, S., and Mann, R.S. (2013). Quantification of gait parameters in freely walking wild type and sensory deprived *Drosophila melanogaster*. eLife *2*, e00231.

Milde, J.J., Seyan, H.S., and Strausfeld, N.J. (1987). The neck motor system of the fly Calliphora erythrocephala - II. Sensory organization. J. Comp. Physiol. A *160*, 225–238.

Namiki, S., and Kanzaki, R. (2016). Comparative neuroanatomy of the lateral accessory lobe in the insect brain. Front. Physiol. *7*, 244.

Nern, A., Pfeiffer, B.D., and Rubin, G.M. (2015). Optimized tools for multicolor stochastic labeling reveal diverse stereotyped cell arrangements in the fly visual system. Proc. Natl. Acad. Sci. USA *112*, E2967–E2976.

Niell, C.M., and Stryker, M.P. (2010). Modulation of visual responses by behavioral state in mouse visual cortex. Neuron *65*, 472–479.

O'Sullivan, A., Lindsay, T., Prudnikova, A., Erdi, B., Dickinson, M., and von Philipsborn, A.C. (2018). Multifunctional wing motor control of song and flight. Curr. Biol. *28*. 2705.e4–2717.e4.

Orlovsky, G.N., Deliagina, T.G., and Grillner, S. (1999). Neuronal Control of Locomotion: From Mollusk to Man (Oxford University Press).

Otsuna, H., Ito, M., and Kawase, T. (2018). Color depth MIP mask search: a new tool to expedite Split-GAL4 creation. Preprint at bioRxiv. https://doi.org/10.1101/318006.

Palmer, C.R., and Kristan, W.B. (2011). Contextual modulation of behavioral choice. Curr. Opin. Neurobiol. *21*, 520–526.

Parker, P.R.L., Brown, M.A., Smear, M.C., and Niell, C.M. (2020). Movement-related signals in sensory areas: roles in natural behavior. Trends Neurosci. *43*, 581–595.

Pierantoni, R. (1976). A look into the cock-pit of the fly. The architecture of the lobular plate. Cell Tissue Res. *171*, 101–122.

Pologruto, T.A., Sabatini, B.L., and Svoboda, K. (2003). ScanImage: flexible software for operating laser scanning microscopes. Biomed. Eng. OnLine *2*, 13.

Rayshubskiy, A., Holtz, S., D'Alessandro, I., Li, A., Vanderbeck, Q., Haber, I., Gibb, P., and Wilson, R. (2020). Neural circuit mechanisms for steering control in walking Drosophila. BioRxiv, 1–50.

Reiser, M.B., and Dickinson, M.H. (2008). A modular display system for insect behavioral neuroscience. J. Neurosci. Methods *167*, 127–139.

Rister, J., Pauls, D., Schnell, B., Ting, C.Y., Lee, C.H., Sinakevitch, I., Morante, J., Strausfeld, N.J., Ito, K., and Heisenberg, M. (2007). Dissection of the peripheral motion channel in the visual system of *Drosophila melanogaster*. Neuron *56*, 155–170.

Rohlfing, T., and Maurer, C.R. (2003). Nonrigid image registration in shared-memory multiprocessor environments with application to brains, breasts, and bees. IEEE Trans. Inf. Technol. Biomed. *7*, 16–25.

Saleem, A.B., Ayaz, A., Jeffery, K.J., Harris, K.D., and Carandini, M. (2013). Integration of visual motion and locomotion in mouse visual cortex. Nat. Neurosci. *16*, 1864–1869.

Scheffer, L., Xu, C.S., Januszewski, M., Lu, Z., Takemura, S., Hayworth, K., Huang, G., Shinomiya, K., Maitin-Shepard, J., Berg, S., et al. (2020). A connectome and analysis of the adult *Drosophila* central brain. eLife *9*, e57443.

Schnell, B., Joesch, M., Forstner, F., Raghu, S.V., Otsuna, H., Ito, K., Borst, A., and Reiff, D.F. (2010). Processing of horizontal optic flow in three visual interneurons of the Drosophila brain. J. Neurophysiol. *103*, 1646–1657.

Schnell, B., Weir, P.T., Roth, E., Fairhall, A.L., and Dickinson, M.H. (2014). Cellular mechanisms for integral feedback in visually guided behavior. Proc. Natl. Acad. Sci. USA *111*, 5700–5705.

Seelig, J.D., Chiappe, M.E., Lott, G.K., Dutta, A., Osborne, J.E., Reiser, M.B., and Jayaraman, V. (2010). Two-photon calcium imaging from head-fixed *Drosophila* during optomotor walking behavior. Nat. Methods *7*, 535–540.

Shadmehr, R., Smith, M.A., and Krakauer, J.W. (2010). Error correction, sensory prediction, and adaptation in motor control. Annu. Rev. Neurosci. *33*, 89–108.

Stone, T., Webb, B., Adden, A., Weddig, N. Ben, Honkanen, A., Templin, R., Wcislo, W., Scimeca, L., Warrant, E., and Heinze, S. (2017). An anatomically constrained model for path integration in the bee brain. Curr. Biol. *27*. 3069.e11–3085.e11.

Straka, H., Simmers, J., and Chagnaud, B.P. (2018). A new perspective on predictive motor signaling. Curr. Biol. *28*, R232–R243.

Strausfeld, N.J. (1976). Atlas of an Insect Brain (Springer-Verlag).

Strausfeld, N.J., and Bacon, J.P. (1983). Multimodal convergence in the central nervous system of dipterous insects. Fortschr. Zool. *28*, 47–76.

Suter, B.A., O'Connor, T., Iyer, V., Petreanu, L.T., Hooks, B.M., Kiritani, T., Svoboda, K., and Shepherd, G.M. (2010). Ephus: multipurpose data acquisition software for neuroscience experiments. Front. Neural Circuits *4*, 100.

Suver, M.P., Mamiya, A., and Dickinson, M.H. (2012). Octopamine neurons mediate flight-induced modulation of visual processing in *Drosophila*. Curr. Biol. *22*, 2294–2302.

Szczecinski, N.S., Bockemühl, T., Chockley, A.S., and Büschges, A. (2018). Static stability predicts the continuum of interleg coordination patterns in *Drosophila*. J. Exp. Biol. *221*, jeb189142.

Tammero, L.F., and Dickinson, M.H. (2002). The influence of visual landscape on the free flight behavior of the fruit fly *Drosophila melanogaster*. J. Exp. Biol. *205*, 327–343. https://doi.org/10.1242/jeb.205.3.327.

Tuthill, J.C., and Azim, E. (2018). Proprioception. Curr. Biol. *28*, R194–R203.

Vinepinsky, E., Cohen, L., Perchik, S., Ben-Shahar, O., Donchin, O., and Segev, R. (2020). Representation of edges, head direction, and swimming kinematics in the brain of freely-navigating fish. Sci. Rep. *10*, 14762.

von Reyn, C.R., Breads, P., Peek, M.Y., Zheng, G.Z., Williamson, W.R., Yee, A.L., Leonardo, A., and Card, G.M. (2014). A spike-timing mechanism for action selection. Nat. Neurosci. *17*, 962–970.

Wirtshafter, H.S., and Wilson, M.A. (2019). Locomotor and hippocampal processing converge in the lateral septum. Curr. Biol. *29*. 3177.e3–3192.e3.

Wittlinger, M., Wehner, R., and Wolf, H. (2006). The ant odometer: stepping on stilts and stumps. Science *312*, 1965–1967.

Wolpert, D.M., and Ghahramani, Z. (2000). Computational principles of movement neuroscience. Nat. Neurosci. *3* (*Suppl*), 1212–1217.

Wosnitza, A., Bockemühl, T., Dübbert, M., Scholz, H., and Büschges, A. (2013). Inter-leg coordination in the control of walking speed in *Drosophila*. J. Exp. Biol. *216*, 480–491.

STAR★METHODS

KEY RESOURCES TABLE

REAGENT or RESOURCE	SOURCE	IDENTIFIER
Antibodies		
Mouse monoclonal anti-nc82	DSHB	Cat # nc82; RRID:AB_2314866
Rabbit polyclonal anti-GFP	Thermo Fisher Scientific	Cat # A6455; RRID: AB_221570
Alexa Fluor 633 conjugated goat anti-mouse	Thermo Fisher Scientific	Cat # A21050; RRID: AB_2535718
Alexa Fluor 488 conjugated goat anti-rabbit	Thermo Fisher Scientific	Cat # A11008; RRID: AB_143165
Rabbit monoclonal anti-HA	Cell Signaling Technologies	Cat # 3724S; RRID:AB_1549585
Rat monoclonal anti-FLAG	Novus Biologicals	Cat # NBP1-06712; RRID: AB_1625981
Alexa Fluor 594 conjugated goat anti-rabbit	Thermo Fisher Scientific	Cat # A-11012; RRID:AB_2534079
Alexa Fluor 647 conjugated goat anti-rat	Thermo Fisher Scientific	Cat # A-21247; RRID:AB_141778
Alexa Fluor 488 conjugated goat anti-mouse	Thermo Fisher Scientific	Cat # A28175; RRID:AB_2536161
Mouse monoclonal anti V5-tag:DyLight®550	Bio-Rad	Cat # MCA1360D550GA; RRID: AB_2687576
Chemicals, peptides, and recombinant proteins		
Histamine	Sigma	Cat # H7125
All trans-retinal	Sigma	Cat # R2500
Collagenase IV	Worthington	Cat # CLS-4
Biocytin hydrazide	Thermo Fisher Scientific	Cat # B1603
Alexa Fluor 568 Hydrazide	Thermo Fisher Scientific	Cat # A10437
PFA	Electron Microscopy Sciences	Cat # 15710
Normal mouse serum	Jackson Immuno Research Laboratories	Cat # 015-000-120
Normal goat serum	Life Technologies	Cat # PCN5000
Vectashield	Vector Laboratories	Cat # H-1200
Deposited data		
Custom MATLAB codes	This paper	https://github.com/ChiappeLab/Analysis-Walking-Stride-Modulation
Experimental models: Organisms/strains		
Drosophila melanogaster: w^{+}; UAS-Ort; +	Rister et al., 2007	N/A
Drosophila melanogaster: w; UAS-2xEGFP; +*	Bloomington Drosophila Stock Center (BDSC)	RRID: BDSC_6874
Drosophila melanogaster: w^{1118}; +; VT058487-GAL4	Vienna Drosophila Resource Center (VDRC)	N/A
Drosophila melanogaster: wDL	Tammero and Dickinson, 2002	N/A
Drosophila melanogaster: w^{1118}; +; R81G07-GAL4	BDSC	RRID: BDSC_40122
Drosophila melanogaster: w, NorpA[36]*	BDSC	RRID: BDSC_9048
Drosophila melanogaster: w^{1118}; +; 20XUAS-IVS-CsChrimson.mVenus	BDSC	RRID: BDSC_55136
Drosophila melanogaster: w^{1118}; R39E01-lexA; +	BDSC	RRID: BDSC_52776
Drosophila melanogaster: y1 w; 13XLexAop2-6XGFP(VK00018)/CyO; Dr1/TM6C, Sb1 Tb1*	BDSC	RRID: BDSC_52265
Drosophila melanogaster: y1 w*; wgSp-1/CyO; 20XUAS-6XGFP(attp2)	BDSC	RRID: BDSC_52262
Drosophila melanogaster: w^{1118}; R11H10-p65.AD(attp40); VT025925-ZpGal4DBD(attp2)	Bidaye et al., 2020 and Salil Bidaye	N/A

(*Continued on next page*)

Continued

REAGENT or RESOURCE	SOURCE	IDENTIFIER
Drosophila melanogaster: w, 5-40-GAL4; dacREFLP;+	Giorgianni and Mann, 2011; Hughes and Thomas, 2007 and César S Mendes	N/A
Drosophila melanogaster: w; UAS-FRT-stop-FRT-TNT/Cyo; +*	BDSC	RRID: BDSC_67690
Drosophila melanogaster: w^{1118}; R27B03-p65.AD(attp40); +	BDSC	RRID: BDSC_70164
Drosophila melanogaster: w^{1118}; +; VT058488-GAL4.DBD(attp2)	BDSC	RRID: BDSC_72871
Drosophila melanogaster: w^{1118}; p65-AD.empty(attp40); GAL4-DBD.empty(attp2)	BDSC	RRID: BDSC_79603
Drosophila melanogaster: w; +; UAS-ReaChR(VK00005)*	BDSC	RRID: BDSC_53749
Drosophila melanogaster: w^{1118}; R46A02-p65.AD(attp40); +	BDSC	RRID: BDSC_71064
Drosophila melanogaster: w^{1118}; R34E09-p65.AD(attp40); VT023823-GAL4.DBD(attp2)/TM6B	BDSC	RRID: BDSC_86632
Drosophila melanogaster: wDL; wDL; 10XUAS-IVS-eGFPKir2.1(attP2)	von Reyn et al., 2014 and Gwyneth Card	N/A
Drosophila melanogaster: w^{1118}; UAS-sytGCaMP6s (attp40)/Cyo; TM2/TM6B	Cohn et al., 2015 and Vanessa Ruta	N/A
Drosophila melanogaster: w^{1118}; +; UAS-CD4-Tdtomato(VK00033)	BDSC	RRID: BDSC_35837
Drosophila melanogaster: w^{1118}, hs-FLPG5.PEST; +; 10xUAS(FRT.stop)myr::smGdP-HA (VK00005), 10xUAS(FRT.stop)myr::smGdP-V5-THS-10xUAS (FRT.stop)myr::smGdP-FLAG(su(Hw)attP1)	BDSC	RRID: BDSC_64085
Software and algorithms		
MATLAB	The Mathworks	https://www.mathworks.com
JAABA	Kabra et al., 2013	http://jaaba.sourceforge.net
DeepLabCut	Mathis et al., 2018	https://github.com/DeepLabCut
Ephus	Suter et al., 2010	http://scanimage.vidriotechnologies.com/display/ephus/Ephus
ScanImage	Pologruto et al., 2003	http://scanimage.vidriotechnologies.com/display/ephus/ScanImage
NeuPrint	Scheffer et al., 2020	https://neuprint.janelia.org
Computational Morphology Toolkit (CMTK)	Rohlfing and Maurer, 2003	https://www.nitrc.org/projects/cmtk/
Natverse	Bates et al., 2020	https://natverse.org
Color-Depth MIP	Otsuna et al., 2018	https://www.janelia.org/open-science/color-depth-mip
DeepEthogram	Bohnslav et al., 2021	https://github.com/jbohnslav/deepethogram

RESOURCE AVAILABILITY

Lead contact

Further information and requests for resources and reagents should be directed to and will be fulfilled by the lead contact, Eugenia Chiappe (eugenia.chiappe@neuro.fchampalimaud.org)

Materials availability

All materials in this study including fly lines and custom tools will be available upon request directed to the lead contact.

Data and code availability

- Data reported in this paper have been deposited at Zenodo and are publicly available (https://doi.org/10.5281/zenodo.6365304).

- All original code has been deposited at the Chiappe lab Github and is publicly available. The link is listed in the key resources table.
- Any additional information required to reanalyze the data reported in this paper is available from the lead contact upon request.

EXPERIMENTAL MODEL AND SUBJECT DETAILS

Flies (*Drosophila melanogaster*) were reared in standard medium at 25°C with a 12-hr light and 12-hr dark cycle. We noticed that male flies have more robust walking behavior on the ball than females. For this reason, we randomly selected male flies for all experiments. We excluded flies that looked unhealthy at the time of the fly preparation, or that displayed less than 10 walking bouts. Overall, this represented about 35% of flies that were discarded for spontaneous walking experiments, and 30% under opto-runs. For the leg mechanosensory perturbation experiments, because of the likely function of these sensory neurons in maintaining coordinated locomotion, many flies walked poorly and never reached the high-speed walking (>5 mm/s for at least 30s, 0.12 g weight of the ball), and we needed to exclude about 70% of flies. For the remaining 30% of flies with this genotype, individual flies displayed walking bouts at high speed that conformed with the threshold criteria. For optogenetic experiments, flies (including controls) were fed with 1 mM all-trans-retinal after eclosion and were kept subsequently in darkness until the experiment. All the experiments were performed with 1-to-4-day-old male flies. Specific sources of transgenic lines are listed in the key resources table.

METHOD DETAILS

Detailed fly genotypes used by figures

Figures 1C, 1F, 2B–2D, S1A, S4F, and S4K:
w^{1118}; UAS-2xEGFP; VT058487-GAL4
Figures 1C, 2B–2D, S4F, and S4K:
w^{DL}; UAS-2xEGFP; R81G07-GAL4
Figures 1D, 1E, and S1:
w^{1118}; UAS-ort/UAS-2xEGFP; +/VT058487-GAL4
Figures 2E–2G, 3A–3C, 3E, 3F, 4E, 4F, 5, 8A–8D, S2B–S2L, S3, S4A–S4E, S6, and S8:
w, NorpA[36]; R39E01-LexA, 13xLexAop2-6xGFP/R11H10-AD; 20xUAS-CsChrimson.mVenus/VT025925-DBD
Figures 4B, 4C, 6A–6C, 8E–8G, and S5:
w, 5-40-GAL4; dacREFLP/UAS-FRT-stop-FRT-TNT; +
w, 5-40-GAL4; dacREFLP; +
Figures 6D–6M: w, NorpA[36]; R27B03-AD/+; VT058488-DBD/UAS-ReaChR
Figures 6F and 6G: w, NorpA[36]; AD.empty/+; DBD.empty/UAS-ReaChR
Figure 7B:
w, NorpA[36]; R39E01-LexA, 13xLexAop2-6xGFP/R46A02-AD; 20xUAS-csChrimson.mVenus/VT023823-DBD.
w, NorpA[36]; R39E01-LexA, 13xLexAop2-6xGFP/R46A02-AD; VT023823-DBD/MKRS
Figures 7C and 7D:
w^{1118}; R39E01-LexA, 13xLexAop2-6xGFP/R46A02-AD; 10XUAS-IVS-eGFPKir2.1/VT023823-DBD
w^{1118}; R39E01-LexA, 13xLexAop2-6xGFP/R46A02-AD; +/VT023823-DBD (GAL4 control)
w^{1118}; R39E01-LexA, 13xLexAop2-6xGFP/AD.empty; 10XUAS-IVS-eGFPKir2.1/DBD.empty (UAS control)
Figures 7E–7I:
w^{1118}; UAS-sytGCaMP6s/R46A02-AD; UAS-CD4-tdTomato/VT023823-DBD
Figure S2A:
w^{1118}; +/R11H10-AD; 20xUAS-CsChrimson.mVenus/VT025925-DBD
Figures S7A and S7C:
w^{1118}; UAS-2xEGFP/R46A02-AD; +/VT023823-DBD
Figure S7B:
w^{1118}, hs-FLPG5.PEST; +/R46A02-AD; 10xUAS(FRT.stop)myr::smGdP-HA, 10xUAS(FRT.stop)myr::smGdP-V5-THS-10xUAS(FRT.stop)myr::smGdP-FLAG/VT023823-DBD

Electrophysiological and calcium recordings

Details of the fly preparation for simultaneous physiology and behavior, and the treadmill system are described in (Fujiwara et al., 2017; Seelig et al., 2010). Briefly, a cold-anesthetized fly was mounted on a custom-made holder, and the back of the head's cuticle was removed with fine tweezers. The dissected fly was mounted under the microscope and positioned on an air-suspended 9 mm diameter ball. *In vivo*, whole-cell patch-clamp recordings and calcium imaging were performed using an upright microscope (Movable Objective Microscope, Sutter) with a 40× water-immersion objective lens (CFI Apo 40XW NIR, Nikon). The external solution, which perfused the preparation constantly, contained 103 mM NaCl, 3 mM KCl, 5 mM TES, 8mM trehalose, 10 mM glucose,

26 mM $NaHCO_3$, 1 mM NaH2PO_4, 4 mM $MgCl_2$ and 1.5 mM $CaCl_2$ (pH 7.3 when equilibrated with 95% O_2/ 5% CO_2; 270–280 mOsm). Patch pipettes (5–7 MΩ) were filled with an internal solution containing 125 mM aspartic acid, 10 mM HEPES, 1 mM EGTA, 1 mM KCl, 4 mM MgATP, 0.5 mM Na_3GTP, 20 μM Alexa 568–hydrazide-Na and 13 mM biocytin hydrazide (pH 7.3; 260–265 mOsm). The neural lamella was ruptured by the local application of collagenase IV (Maimon et al., 2010). Current-clamp data were filtered at 4 kHz, digitized at 10 kHz using a MultiClamp700B amplifier (Molecular Devices), and acquired with Ephus. The recorded cell membrane potential (Vm) was corrected for junction potential (11 mV). For HS cell recordings performed in darkness during spontaneous walking (19/25 cells, Figures 1C, 2B–2D, S4F, and S4K) and for HS cell recordings performed under leg mechanosensory neurons' perturbations, (Figures 4B, 4C, 6A–6C, 8E–8G, and S5), data was obtained during a previous study (Fujiwara et al., 2017). Synaptic activity from leg mechanosensory neurons was inactivated by the selective expression of UAS-FRT-stop-FRT-TNT in the leg imaginal disc (dac^{RE}-FLP, (Giorgianni and Mann, 2011)), driven by 5-40-GAL4, a pan sensory neuron driver (Hughes and Thomas, 2007). The rest of the data was collected during this study.

We recorded internal calcium dynamics from the axons of LAL-PS-AN_{contra} projecting at the PS, the neuron's most superficial projection field, using a custom-built 2-photon laser scanning system. We used a Chameleon Ultra II Ti-Sapphire femtosecond laser (Coherent) tuned to 930 nm for GCaMP excitation (6 mW under the objective lens). Emission was collected on GaAsP PMT detectors (Hamamatsu, H10770PA-40) through a 535/50 nm bandpass filter (Chroma). A 128×128 pixels slice image was acquired at 15 Hz with ScanImage.

Chemogenetic silencing of HS cells

An electrode filled with external ringer solution containing 1 mM histamine and 40 μM Alexa 568 was placed in juxtaposition to the axon terminal of GFP-tagged HS cells guided by 2-photon imaging. The neural activity manipulation was conditional to the fly's forward velocity *via* a closed-loop system. Real-time treadmill signals (<10ms delay) were detected with a panel display controller unit (IO Rodeo, Reiser and Dickinson, 2008). Once the forward velocity reached a threshold (>1 mm/s on average for 3s), brief pulses of histamine (10ms, 6 psi) were applied. Control flies with no artificial expression of ort showed minimal inhibition upon histamine application (Figures 1F and S1A), indicating that HS cells do not express high levels of ort endogenously. In contrast, brief pulses of histamine induced a reliable hyperpolarization in HS cells expressing ort (-11.9±0.72 mV at the peak, mean±SEM, n=12 cells).

Injecting 1mM histamine at the HS-cell axon terminals also induced a slight but measurable inhibition in VS cells (-2.8±0.8 mV n=5 cells, Mean±SEM) that could contribute to the overt effect on steering of the walking fly. To test the contribution of VS cells to behavior, we examined the fly's behavior when we applied histamine directly onto VS instead of HS axons using the same GAL4 driver. For this purpose, we adjusted the histamine concentration in the solution (300 μM) to induce inhibition in VS cells with a magnitude that was comparable or slightly higher than the one observed when targeting HS axons (-5.8±1.0 mV, n=6 cells, Mean±SEM). Directly inhibiting VS cells in this manner induced no overt effect on the walking behavior of the fly under an identical closed-loop configuration between the fly's forward speed and the histamine application (Figure S1C). We therefore concluded that despite the off-target expression of the VT058487-GAL4 line, the results from these experiments altogether support the model that the steering effects are a consequence of the unilateral perturbation of the activity of the population of HS cells.

Optogenetic activation of BPNs or HS cells

Unless otherwise stated, whole-cell patch recordings of HS and VS cells were performed in head-fixed, blind flies (NorpA mutant (Bloomquist et al., 1988)) walking on the spherical treadmill. A fiber-coupled light (617nm, M617, Thorlabs) was projected onto the central part of the brain through the objective lens to activate selectively BPNs expressing UAS-csChrimson. Each trial consisted of 5s of stimulation with light pulsed at 100 Hz (50% duty cycle) and intensity ranging from 42 to 135μW/mm^2. For Figure 7B, ascending neurons were activated with the fiber-coupled light (36 μW/mm^2). Walking movements of the left-side front, middle, and hind legs were simultaneously captured with a monochrome digital camera (UI-3240CP-NIR-GL, iDS), coupled to a 25mm focal length lens (M2514-MP2, Computar), and an extender (EX2C, Computar). Images were acquired at 100Hz by externally triggering individual frames from a data acquisition card (USB-6229, National Instruments). For activating HS cells, the 617nm fiber-coupled light (236 μW/mm^2) was projected onto the right side of the brain similarly through the objective lens targeting right-sided HS cells expressing UAS-ReaChR. To dampen the illumination on the contralateral brain hemisphere, the head cuticle covering this side was kept intact. HS-cell activation was conditional to the fly's forward velocity *via* the above-mentioned closed-loop system; once the forward velocity reached a threshold (>3 mm/s on average for 3s), brief light pulses (50ms) were applied. To promote the fly's forward walking, we heated up around the fly to 29 °C by wrapping a nichrome wire to the aluminum treadmill ball holder and passing current to the wire. To track the lateral movement of a front leg, we installed an additional frontal camera (UI-3240ML-NIR-GL, iDS), coupled to a 1.0X 94mm focal length lens (InfiniStix). Images were acquired at 100Hz as above.

For the subset of recordings labeled as the "Ball stopped" condition (Figures S3A–S3C), the airflow of the spherical treadmill was turned off, thereby making rotations of the ball difficult for the fly. Under this condition, flies stopped locomotion and transitioned into either quiescence or non-locomotive movements. After this "Ball Stopped" condition, the airflow was resumed under the condition labeled as "After". For analysis, we used six trials of each condition per fly-cell pair (Figures S3B and S3C).

To examine whether the fly's forward walking induced by BPNs activation was sensitive to course stabilizing visual feedback (Figure S2A), we presented the head-fixed fly with a visual stimulus (9° random dots, 16% density) using a 32×96 arrays of 570nm green LEDs (Bet Lux Electronics, Reiser and Dickinson, 2008) in unity gain closed-loop with the fly's rotation. To activate

BPNs non-invasively, we placed an optic fiber (200μm core, M25L02, Thorlabs) 5mm apart from the fly's head and illuminated it at 100Hz (10% duty cycle) and average intensity of 20μW/mm^2. Note that the activation strength was turned down to prevent masking the visual stimulus.

HS-cell recording under visual feedback

To examine whether HS cells activity under the presence of visual feedback was also modulated by stride-related signals (Figure 3D), we recorded HS-cell activity under a unity gain of closed-loop translational visual stimulus (9° random dots, 16% density) coupled to the forward velocity of the spontaneously walking fly. The treadmill signal, sampled at 4 kHz, was integrated over 1.6ms and sent to the LED arena controller to control the translational motion in the visual display (the total closed-loop delay < 10ms). Note that in these experiments, we split the visual display in two, centered at the front of the fly to induce the translational feedback condition. That is, the closed-loop configuration was 1D and did not incorporate the rotations of the fly that may otherwise interfere with the visual responses of the cell, masking the presence of the forward-velocity associated oscillations. To compare the stride-related signals in the same individual and cell under different light conditions, the protocol alternated 2 min recordings between visual feedback and darkness.

HS-cell recording with external leg movement

To passively move a leg, we adopted the method described in (Mamiya et al., 2018). Briefly, a tip of a tiny insect pin (12.5μm tip diameter, 26002-10, Fine Science Tools) was inserted into the coxal part of a front leg. A small, rare metal magnet (1x1.5x2 mm, Magnet Solutions) attached to a screw head was placed under the leg and was rotated periodically along the front-back axis of the fly's body with a servomotor (period: 5Hz, amplitude: 20°). The other legs were removed to avoid the contribution of spontaneous leg movements to HS cells' activity.

Immunostaining

Isolated brains were fixed for 30 min at room temperature in 4% paraformaldehyde in PBS, rinsed in PBT (PBS, 0.5% Triton X-100 and 10 mg/ml BSA), and blocked in PBT + 10% NGS for 15min. Brains were incubated in primary antibodies (1:25 mouse nc82 and 1:1000 rabbit antibody to GFP) at 4°C for three days. After several washes in PBT, brains were incubated with secondary antibodies (1:500 goat-anti rabbit: Alexa Fluor 488 and 1:500 goat-anti mouse: Alexa Fluor 633) for three days at 4°C. Brains were mounted in Vectashield, and confocal images were acquired with a Zeiss LSM710 scope with a 40× oil-immersion or 25× multi-immersion objective lens. For the MultiColor FlpOut experiments (Figure S7B), we followed the original protocol described in (Nern et al., 2015), except 10% NGS was used for blocking steps.

QUANTIFICATION AND STATISTICAL ANALYSIS

We used MATLAB (MathWorks, Inc., Natick, MA) for data analysis, neither with specific randomization nor blinding.

Processing of physiology and behavior data

In figure panels, traces were shown with the grand mean ± SEM, unless otherwise noted. Electrophysiological and treadmill signals were down-sampled to 500Hz and smoothed using a lowess algorithm with a 120ms window. To compare neural and velocity signals to leg movements, time series were further down-sampled to 100Hz to match the leg tracking's video sampling rate. Note that down-sampling, filtering, and averaging neural activity degraded the amplitude of neural modulation. Therefore, to examine the amplitude of the modulation (Figures 3C and 4E), we obtained the distribution of the peak-to-trough magnitude of the oscillations within a stride window (from stance onset to the next stance onset) from the original signals. The Vm oscillation within a corresponding short window during stationary periods (i.e., moments with zero treadmill signals before BPNs activation) was calculated to estimate the noise level.

In spontaneous walking bouts (Figures 1C, 2B–2D, S4F, and S4K), walking-related signals in HS cells were analyzed following (Fujiwara et al., 2017). Briefly, we extracted walking bouts from the treadmill signals using a supervised machine-learning algorithm JAABA (Kabra et al., 2013) based on side-view videos of the walking fly. Isolated walking bouts and the corresponding Vm signals were concatenated per fly.

For Figures 1E and 1F, histamine injection triggered traces were divided depending on the mean value of the forward velocity of the fly within a second before histamine application (-1–0s window). Note that in Figures 1E and 1F, the Vm is only reported for recordings that lasted until the end of the experiment (6/11 and 4/9 fly-cell pairs for the experimental and control).

To quantify the change in the course direction of the fly (Figures 1E, 1F, S1A, and S1C), we calculated the mean angular velocity (Va) within a window of 2s before histamine injection and subtracted it from the mean angular velocity within 2s after histamine injection. For brief HS-cell activation experiment (Figures 6F and 6I), mean Va or leg positions between windows of 500ms before and after the light illumination were compared for the quantification. For Figure 6K, first, light illumination-triggered average Va trace was calculated per condition (whether the light was delivered at the swing or stance) and per fly. For each of those average Va traces, the mean and variance within a window of 100ms before light illumination were calculated as the baseline. Then, the behavioral response latency was defined as the time point when the average Va trace first exceeded the mean + 2*SD of the baseline toward ipsilateral steering direction.

For Figure 5B, the change in HS cells' Vm (relative of quiescence, ΔVm), the temporal derivative of Vm, and the Va and Vf were triggered at local peaks (> 1mm/s) of the high-pass filtered Vf (>5Hz, $Vf_{|5Hz}$) during opto-runs. For each fly-cell pair, these

event-triggered segments of data were further classified based on the magnitude of angular drift attenuation, the decrease of Va post Vf peak. If the magnitude of the decrease in Va was within the 1st or 4th quartiles of the distribution across opto-run segments, these classes were labeled as the low vs. high drift attenuation (i.e., no vs. rapid adjustment) conditions, respectively. Drift attenuation (ΔVa post Vf peak) was defined as the mean Va within a 0–200ms window (peak Vf at 0) subtracted from Va at time 0 (at local Vf peak).

For Figure S4F, Vm and Vf were triggered at local peaks/troughs of $Vf_{|5Hz}$ with a threshold of ±1mm/s during left (Va<-50°/s) or right (Va>50°/s) angular drifts. For Figure S4K, $Vf_{|5Hz}$ was projected onto a 2D behavioral map (Va bins: 20°/s, $Vf_{|5Hz}$ bins: 0.3mm/s). The value at each pixel was calculated as the mean of all collected data points.

For Figure S5D, baseline slope (indicated by a dashed black line) was defined by a linear fitting of the PSD plot at 2–3 and 8–9 Hz (outside of the range where stride-related Vm oscillations appear). The strength of stride-related Vm oscillations was defined as the difference (ΔPSD) between the peak of the plot at 3–8 Hz and the baseline.

For Figure S6, "residual drift attenuation", drift attenuation that is independent of the mean magnitude of Va within the preceding 200ms window from Vf peak was calculated as follows:

$$\textit{residual drift attenuation} = \textit{drift attenuation} - (a * \textit{preceding drift} + b)$$

Where *a* is the slope coefficient and *b* is the intercept of the linear regression between the drift attenuation and the preceding mean magnitude of Va. For Figure S6F, the temporal derivative of HS cells' Vm, Va, and Vf were triggered at local peaks of $Vf_{|5Hz}$ as described above, and the triggered traces were classified based on the magnitude of the residual drift attenuation following the same class definition as above.

Leg tracking

We used a machine learning-based strategy (DeepLabCut, (Mathis et al., 2018)) to monitor side-view leg movements by tracking two prominent joints: the femur-tibia and tibia-tarsus. The training was based on manual annotation of these joints in 4 flies (100 frames each, 0.17–0.26% of the total amount of time per fly). The output of the trained network gave the x and y positions of the joints as a function of time. Because flies with manipulated leg mechanosensory neurons showed different patterns of leg movements, a new network was separately trained with data from 4 flies of this genotype. Similarly, for images from the frontal camera, an independent network was trained with data from 4 flies imaged on this view that tracked the x and y positions of a front leg's tip.

To define leg phases, time courses were first divided into 1s chunks. Chunks with Vf > 5mm/s and with consistent periodic leg movements (periodicity of leg positions was estimated by their autocorrelation function, Figure S2G) were used for further analysis (45% of total chunks used). Similarly, for spontaneous walking datasets (Figures 3D, 4B, 4C, 6, 7C, 7D, and 8E–8G), walking events with Vf > 5mm/s and with consistent periodic leg movements were selected (**20**% of chunks used). Local inspection of these chunks with periodic leg movements indicated that the stance onset of the legs corresponded to the local minima (i.e., the forward most position) of the horizontal (x-axis), whereas the swing onset corresponded to the local maxima of the horizontal axis (Figure S2C). Therefore, the stance and swing phases were defined when the x-axis position of the leg shifted from the local minima to the local maxima and vice versa, respectively. Combining the positional information of the femur-tibia and tibia-tarsus joints (by the square root sum of squares of their horizontal positions, Figure S2C) increased the fidelity of the detection of the local maxima and minima in the trajectory. From the frontal view (Figures 6H–6M), the joint trajectory was more complicated, and leg phases were defined by whether the leg's tip overwrapped with the treadmill ball (i.e., stance) or not (i.e., swing) on the image pixel.

Next, phase values were linearly assigned to the swing (0 to π) and stance (π to 2π) periods. Similarly, local maxima and minima of HS cells' Vm were detected, and phase values were assigned to the time series so that the local maxima and minima correspond to 0 and π, respectively. The phase relationship between leg movements and HS cells' Vm (Figure 3E) was characterized by calculating the mean value of the Vm phase subtracted from the leg phase per stride, and the distributions across strides were plotted. For tuning plots, the mean value of the high-pass filtered Vm ($Vm_{|5\ Hz}$) (Figures 3D, 3F, 4B, 4F, 7C, 8B, 8C, 8E, S2F, S2L, S4A, S4D, S5A, S8D, and S8F), the temporal derivative of Vm (Figures 5C, 6A, and S6A) or the $Vf_{|5Hz}$ (Figures S4A, S4D, and S8B) at each leg phase bin of π/4 was calculated. For Figures 4C and 7D, the mean oscillation magnitude was calculated as the difference between the peak and trough of the $Vm_{|5Hz}$ tuning. For Figure 6M, data in each fly was divided per stride depending on whether the stance duration of the stride right before light illumination was shorter (bottom half of the length distribution) or longer (top half). For Figures 8B, 8C, 8E, S8B, S8D, and S8F, data in each recording was divided per stride depending on whether the stance duration was shorter (1st quartile of the length distribution) or longer (4th quartile). Tuning plots were generated with these classified data. For Figures 8C, S8B, and S8F, the mean stance duration over 10 consecutive strides was used for the classification. For Figure S4B, the temporal derivative of Vm was projected onto a 2D leg phase space with a bin of π/4. The value at each pixel was calculated as the mean across all collected data points. For Figures S3D and S5C, high-pass filtered Vm ($Vm_{|5\ Hz}$) was similarly projected onto a 2D tibia-tarsus leg joint trajectory space with a bin of 50μm. For Figure S3D, data in each recording was divided per stride depending on whether the x (horizontal) position of the joint at the stance onset was more anterior (bottom half of the position distribution) or posterior (top half). For Figure S5A, data with high-speed walking (Vf > 5mm/s) was first divided into 3s chunks. Then, the auto correlation coefficient was calculated for x and y positions of the femur-tibia and tibia-tarsus joints (that is, four coefficients in total) per chunk. The x position of the tibia-tarsus joint and its autocorrelation coefficient are shown in Figure S5A 1st and 3rd columns as examples. If the second peak amplitude of the coefficient exceeds 0.5 for all the four coefficient traces, that chunk was considered as the walking event with periodic leg movements and used for further analysis. For each of these extracted chunks, the Vm difference between the

stance and swing onsets in the leg phase tuning curve (Figure S5A 4th column) was calculated, and the distributions were compared between experimental and control flies (Figure S5B).

Simulation

The model has as inputs the leg's stride cycle phases (see below) and Va (Figure S4H). The outputs of the model are HS-cells' Vm and the fly's Vf. For simplification, the model considered the pair of front legs only. A realistic sequence of swing and stance phases for the left and right legs was constructed as follows. A random sequence of stance durations for one leg was initially generated. Following the distribution of swing and stance durations during BPNs activation, which ranged between 30–60ms and 50–150ms, a sequence of swing phases was added with a duration that was proportional to the previous stance duration within a range. Once the swing and stance phases of one leg were defined, the phases for the other leg were generated such that each swing phase was placed within the other leg's stance period (DeAngelis et al., 2019; Mendes et al., 2013; Szczecinski et al., 2018).

Next, for the contralateral leg modulation model configuration (Model 1), Vm was based on the contralateral leg phase such that the fictive HS cell was depolarized from swing onset $(\theta_{min} = 0)$ to early stance phase $\left(\theta_{max} = \frac{5}{4}\pi\right)$ and was hyperpolarized from the early stance phase to the swing onset:

$$\mathrm{V_m}(\theta)\{L|R\} = C_{Vm}(1 + \sin(\theta'(\theta\{R|L\}) + \sigma))$$

where $\mathrm{V_m}(\theta)\{L|R\}$ is a non-negative value of the left or the right HS cell's $\mathrm{V_m}$, $\theta\{R|L\}$ is the right or the left leg phase, θ' is an oscillator with values $-\frac{\pi}{2}$ at θ_{min} and $\frac{\pi}{2}$ at θ_{max}, C_{Vm} is a constant scaling factor to match the scale of modeled traces to the actual data, and σ is a noise parameter.

For the ipsilateral leg modulation model configuration (Model 2), $\mathrm{Vm}(\theta)\{L|R\}$ was calculated with the ipsilateral leg phase $\theta\{L|R\}$ and θ' became $\frac{\pi}{2}$ at θ_{min} and $-\frac{\pi}{2}$ at θ_{max} (i.e., assumption of depolarization during stance).

Based on the observed Vf tuning to the leg phase (Figures S4C and S4D), both the left and right leg phases contributed to Vf in the model, and their specific contribution as a function of the stride cycle was weighted depending on Va. The contribution function of each leg to Vf, $\mathrm{F}(\theta)\{L|R\}$ was defined as:

$$\mathrm{F}(\theta)\{L|R\} = C_{Vf}(1 + \sin(\theta'\{\theta(L|R)\} + \sigma))$$

where θ is the leg phase, θ_{min}, θ_{max}, and σ are shared with $\mathrm{Vm}(\theta)$. C_{Vf} is a constant scaling factor to match the scale to the actual data. Then, the overall $\mathrm{V_f}$ was determined by weighting the magnitude of the angular deviation $(\mathrm{W(Va)})$ to the contribution function of each leg (Figure S4H):

$$\mathrm{V_f}(\theta) = \mathrm{W(Va)} \times \mathrm{F}(\theta)\{R\} + (1 - W(\mathrm{Va})) \times \mathrm{F}(\theta)\{L\}$$

$$\mathrm{W(Va)} = 0.5 + \tanh(Va_{mean} / Va_{EC50})$$

where Va_{mean} is the mean value of the Va over past 100ms, Va_{EC50} (200 °/s) determines the sensitivity of the weight to the Va value (Smaller Va_{EC50} means that $\mathrm{W(Va)}$ reaches close to 1 at smaller Va).

We used the observed Va time series (actual data) for the input of the simulation. Therefore, the length of a simulation matched the length of a recording. We applied this simulation algorithm using each of 25 recording data to generate 50 leg-ipsilateral HS cell's Vm and leg-contralateral HS cell's Vm pairs, and Vf. Then, the simulated Vm tuning to the leg phase (Figure S4I), and simulated 2D behavioral maps (Figure S4J) were plotted using the simulated Vm and Vf time courses.

Ball stop experiment

To compare the effect of the fly's movement during walking vs. non-walking conditions (''Before'', ''Ball Stopped'', ''After'' conditions), for each trial, we extracted a quarter of the total pixels whose intensity varied most over time from the side-view video recordings during BPNs activation. Then, the time course of the pixel intensity was high-pass filtered (> 5Hz) per pixel and averaged across extracted pixels. The autocorrelation coefficient of the filtered, averaged time course was calculated (Figure S3A, bottom). The periodicity strength of the fly' movement (leg motion coupling) was estimated as the standard deviation of the autocorrelation coefficient trace over a window defined by 100–500ms lag. This was necessary since the coefficient of the autocorrelation at lag 0 was always 1 independent of the periodic nature of the pixels change in intensity, and therefore, the coefficient within a time window around lag 0 (0–100ms) were not used. Similarly, the periodicity strength of the corresponding neural activity (Vm coupling) was estimated as the standard deviation of the autocorrelation coefficient of $\mathrm{Vm_{|5Hz}}$over the 100–500ms lag time window. In Figure S3B, each data point represents the mean value of the Vm coupling over 6 trials per fly-cell pair, with bars indicating the grand mean. Figure S3C, shows for all the 6 trials from all fly-cell pairs (n=10) across the 3 conditions (6×10×3=180 data points) the Vm vs. leg motion couplings. Linear regression was performed for these 180 data points.

External leg movement experiment

Using a side view image, the time points when the passive moving leg reached the maximal and minimal horizontal positions were extracted. Like the definition of leg phase during spontaneous walking and opto-runs, fictive stance and swing were defined as when

their positions shifted from the local minima to the local maxima and vice versa, respectively. For Figure 4E, the amplitude of the Vm oscillation within a stride window (from fictive stance onset to the next fictive stance onset) was calculated using raw Vm traces similar to Figure 3C.

Calcium imaging

XY motion was corrected using an algorithm described in (Guizar-Sicairos et al., 2008). Relative fluorescence changes (ΔF/F) were calculated with respect to the baseline fluorescence during quiescence. Region of interests were defined as those pixels with mean intensities over a trial (120 s) 2 SD brighter than the average of all pixels. For calculating the cross-covariance and the walking velocity tuning (Figures 7F and 7G), treadmill signals were down-sampled to the imaging scanning rate (15 Hz). Based on the time lag in the cross-covariance (Figure 7F, +666 ms), the walking velocity tuning was plotted with the lagged calcium response (Va bins: 40°/s vs. Vf bins: 1mm/s, Figure 7G). The value at each pixel was calculated as the mean of all the collected data points. To extract walking and front leg grooming events (Figures 7H and 7I), we annotated a fly's side-view video using a deep learning-based algorithm, DeepEthogram (Bohnslav et al., 2021). Considering the slow kinetics of calcium activity, walking or grooming events lasting over 500ms were selected, and the mean calcium response in each event was used for the analysis.

Anatomy

A confocal image of the AN split-GAL4 driver was registered onto the JRC2018 unisex brain template (Bogovic et al., 2020) using the CMTK toolkit and then converted into a Color-Depth MIP image (Figure S7C) (Meissner et al., 2020). A Color-Depth MIP image for the corresponding neuron in the hemibrain was generated using the Natverse toolkit (Bates et al., 2020). The shortest synaptic paths were analyzed on NeuPrint (Clements et al., 2020) (Figure S7E).

Statistics

We used MATLAB for statistics. We performed a two-sided Wilcoxon signed-rank test (i.e., signed-rank test) for paired groups, a two-sided Wilcoxon rank-sum test (i.e., rank-sum test) for comparisons between two independent groups, and Kruskal-Wallis followed by a Tukey-Kramer test for multiple comparisons. For statistics in Figure 1C, 1% of all data was randomly chosen (bootstrap) to fit linear regression, and the offset of the fitted line was measured. This procedure was performed both in low vs. high forward speed conditions, and the offset difference was calculated. This was repeated 1000 times to obtain a distribution for the offset difference. The p-value was determined by counting how many data points (out of 1000) crossed the zero value. Similarly, for Figure 8G, the offset difference was calculated for the experimental and control groups, and the p-value was determined by counting how many times (out of 1000 repetitions) the offset value for the experimental was larger than the one for the control. In most cases, n represents the number of cells or animals (a single neuron was recorded from one animal, typically noted as fly-cell pairs). For other cases, n represents the number of trials within a cell/animal or across cells/animals. Importantly, the definition of the value of n is presented always whenever it appears to avoid confusion. Unless otherwise noted, the center and dispersion of the data were shown as the mean and SEM. The statistical details and the exact value of n in each experiment can be found in the Results or in the figure legends.

Neuron, Volume *110*

Supplemental information

Walking strides direct rapid and flexible recruitment of visual circuits for course control in *Drosophila*

Terufumi Fujiwara, Margarida Brotas, and M. Eugenia Chiappe

Figure S1 (related to Figure 1): HS cells but not VS cells contribute to steering

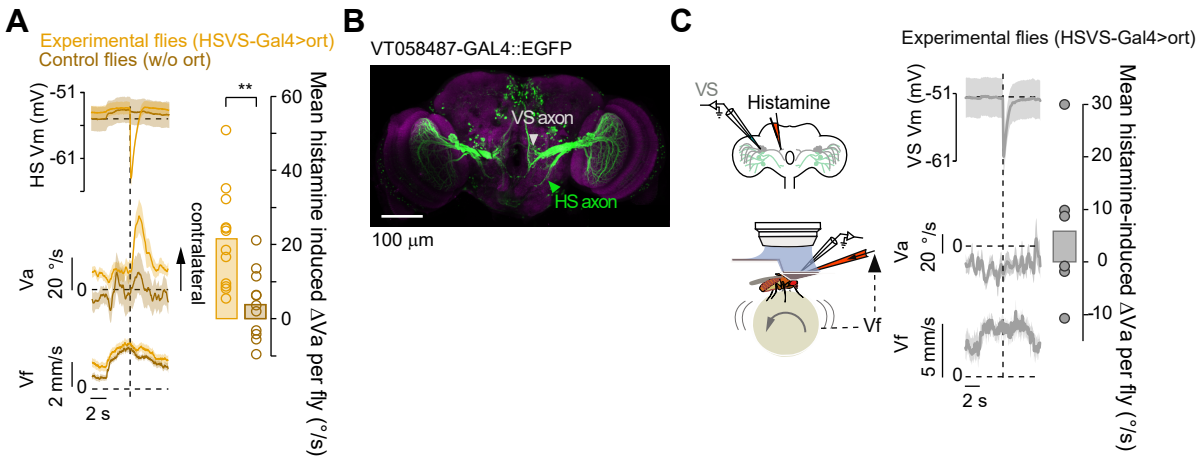

Figure S1 (related to Figure 1): HS but not VS cells contribute to steering. (**A**) Left, Vm, Va, and Vf traces (grand mean ± SEM) in experimental (orange, n=12 flies) or control flies (without exogenous Ort expression, maroon, n=11 flies) triggered at histamine application. Right, mean histamine-induced change in Va (ΔVa) per fly in experimental vs. control flies (p=0.0023, Z=3.05, Wilcoxon rank-sum test). Note that Vm is reported for a subset of flies in which the whole-cell condition lasted until the end of the experiment (7/12 and 6/11 fly-cell pairs for experimental and control flies, respectively). (**B**) Confocal image stack of the VT058487 line driving the expression of EGFP. HS-(green) and VS-cell (light gray) axon terminals are indicated with arrowheads. (**C**) Left, histamine was injected at the axon terminals of VS cells while their activity was monitored by whole-cell patch recordings in flies walking at high speed. Middle, Vm, Va, and Vf triggered at histamine application (n=6 flies, grand mean ± SEM). Note that Vm is reported only for recordings that lasted until the end of the experiment (5/6 fly-cell pairs). Right, mean histamine-induced ΔVa per fly (before injection: -25.8±6.8 °/s vs. after injection: -20.0±8.1 °/s, p=0.69, Wilcoxon signed-rank test, n=6 flies).

Figure S2 (related to Figure 3): Leg movements and their correlation with neural activity and forward velocity

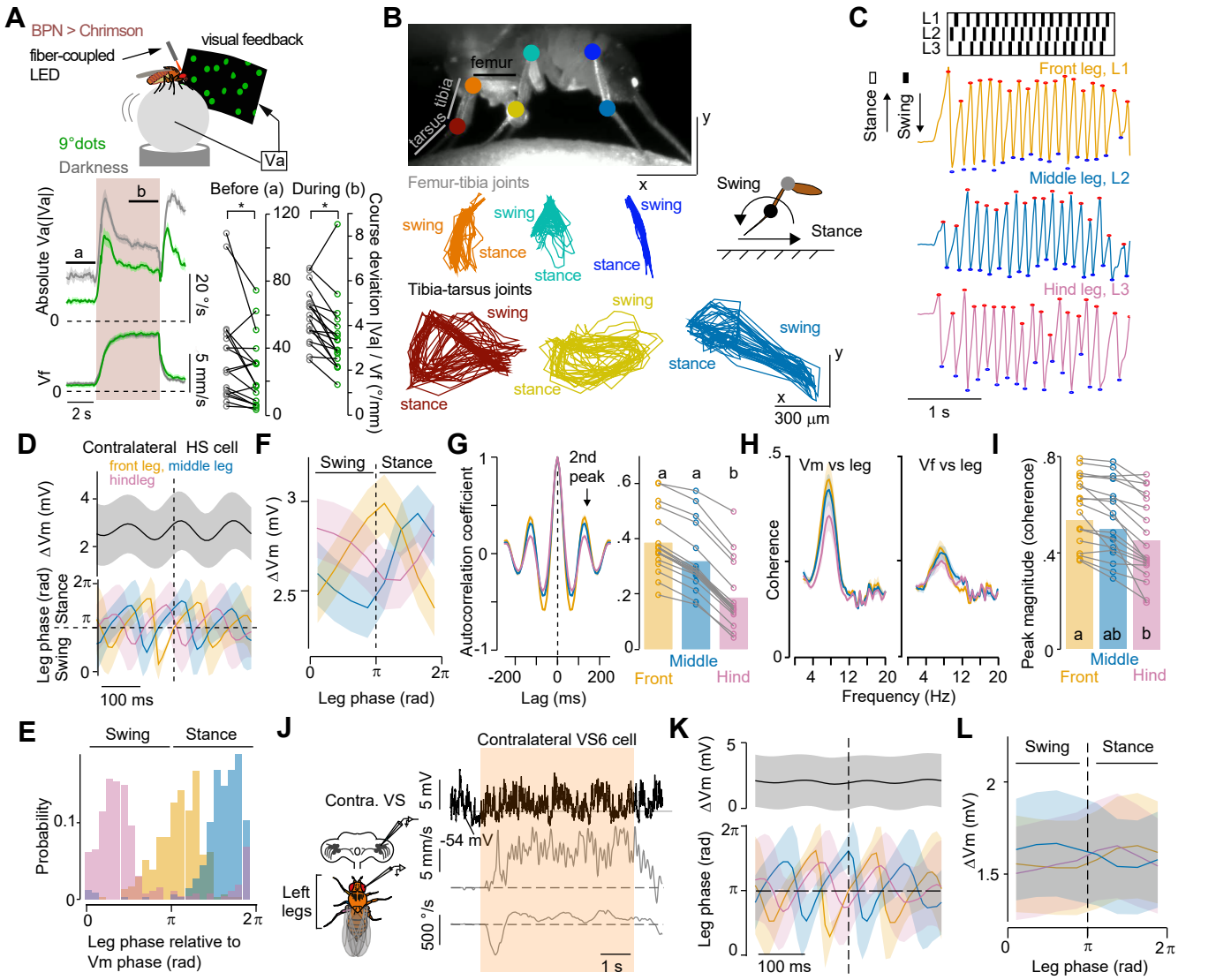

Figure S2 (related to Figure 3): Leg movements and their correlation with neural activity and forward velocity. (**A**) Top, schematic of the experimental closed-loop configuration between the fly's Va and the visual stimuli ("visual feedback", bright green random dots of size 9°, see **STAR Methods**). Bottom, the absolute Va (top, |Va|) and Vf (middle) velocity of flies walking in darkness (gray) or in the presence of visual feedback (green, grand mean ± SEM, n=18 flies). The shaded area indicates the period of optogenetic activation of BPNs, the black line shows the time used for analysis: before (a) and during (b) optogenetic stimulation. Right, mean course deviation, |Va|/Vf, before and during activation of BPNs (black bar) in flies walking in darkness (black) or under the presence of visual feedback (green) (before activation: p=0.016, Z=2.42; during activation: p=0.022, Z=2.29, Wilcoxon signed-rank test). (**B**) Top, side view of an example fly with markers on the femur-tibia and tibia-tarsus joints labeled with DeepLabCut. Bottom, example trajectories of the joints over the stride during a 5s activation of BPNs. Color code indicates the specific leg. (**C**) Top, the swing and stance phases of the three left legs. Bottom, corresponding time courses of the combined x-position of the femur-tibia and tibia-tarsus joints (see **STAR Methods**). Red and blue markers indicate local maxima and minima of the position, corresponding to the onset of swing and stance, respectively. (**D**) Mean ΔVm and leg phases triggered at the stance onset of the left front leg (example fly, n=454 stance onsets). Shaded areas indicate SD. (**E**) Probability distribution of leg phases relative to the phase of Vm oscillations for the example in (**D**). Phase values from 0 to π and from π to 2π correspond to the swing and stance periods of the cycle, respectively. (**F**) HS cells tuning to the contralateral front (orange), middle (blue), and hind (pink) leg movements (grand mean ± SEM, n=19 fly-cell pairs). (**G**) Left, coefficient of autocorrelation of leg movements. Color code: same as in (**B**). Right, amplitude of the coefficient for the second peak in each leg. Letters indicate a significant difference (P<0.05, H=22.56, Kruskal-Wallis followed by Tukey Kramer test, n=19 flies). (**H**) Magnitude-squared coherence between leg movements and Vm (left), and between leg movements and Vf (right) (n=19 fly-cell pairs). (**I**) Magnitude of the coherence peak between leg movement and Vm to each leg (P<0.05, H=6.32, Kruskal-Wallis followed by Tukey Kramer test, n=19 fly-cell pairs). (**J**) Left, schematic of the recorded neural activity and leg movements. Right, example time series of a right VS6 cell's Vm (top), the fly's Vf (middle) and Va (bottom) during activation in BPNs (orange shaded area). (**K**) Mean ΔVm and leg phases triggered at the left front leg's stance onset in the same example. Shaded areas indicate SD (n=775 stance onsets). (**L**) Tuning of contralateral VS cells' Vm to the front (orange), middle (blue), and hind (magenta) leg phases (n=7 fly-cell pairs).

Figure S3 (related to Figure 3): Stride-coupled membrane potential oscillations in HS cells are not induced by activation of BPNs *per se* and reflect actual leg movements

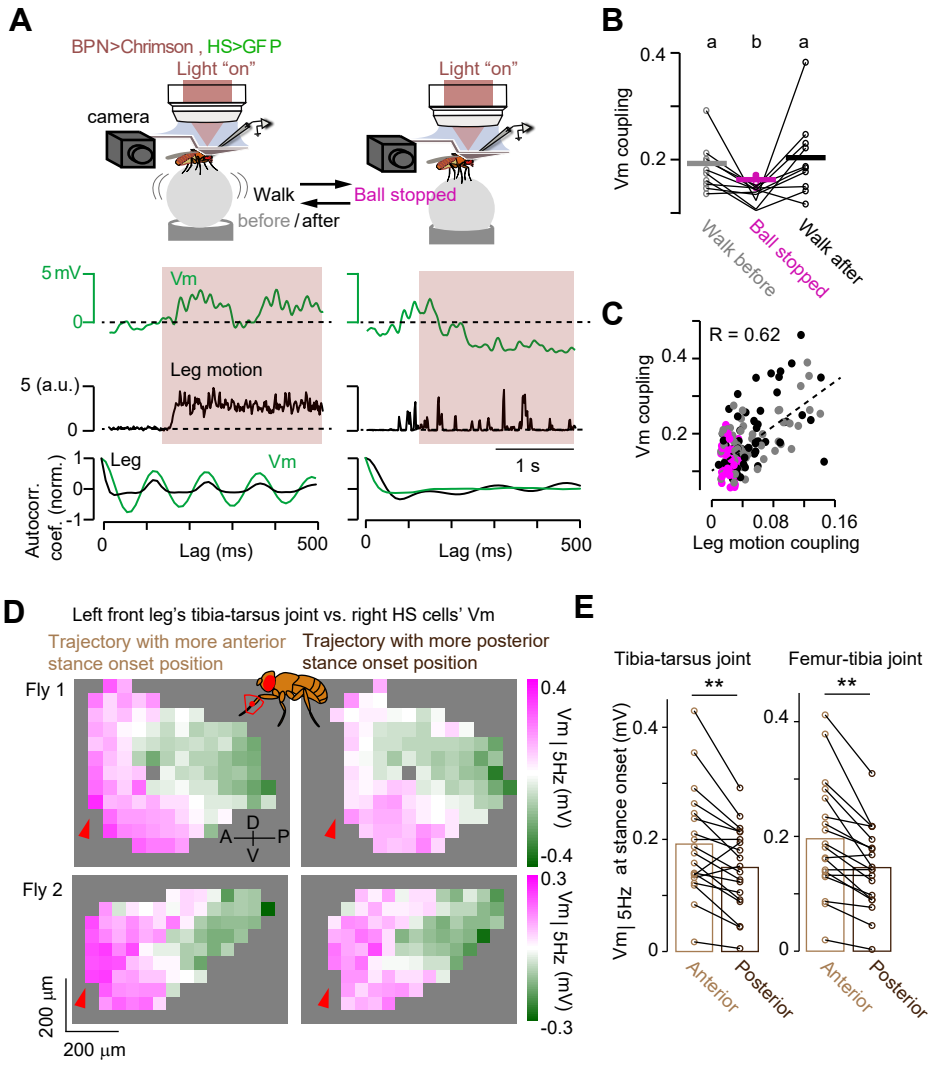

Figure S3 (related to Figure 3): Stride-coupled membrane potential oscillations in HS cells are not induced by activation of BPNs *per se* and reflect actual leg movements. (**A**) Top, schematic of the experimental design. Whole cell-patch recordings from HS cells in simultaneous with optogenetic activation of BPNs (red shadow, "lights on") in walking ("walk", left) or not-walking ("ball stopped", right) flies. The latter condition was induced by stopping the air flow of the ball; note that this manipulation was reversible. To monitor behavior under these conditions, overall leg motion was extracted from the camera tracking legs (see **STAR Methods**). Middle, time series of Vm and the combined leg motion signal. Bottom, normalized autocorrelation coefficient as a function of lag for the neural activity dynamics (Vm, green) and the leg motion signal (leg, black). The oscillatory profile of the autocorrelation for the leg motion signal is characteristic of the periodic nature of walking. (**B**) Quantification of the neural activity autocorrelation strength (Vm coupling) before, during, and after stopping the ball. Letters above the plot indicate significant differences ($p<0.05$, Kruskal-Wallis followed by Tukey Kramer test, $Z=11.34$, $n=10$ fly-cell pairs). (**C**) Correlation between the autocorrelation strength of the fly's leg movements (leg motion coupling) and Vm coupling in each trial. The dashed line shows the linear regression of all the points ($n=180$ trials). (**D**) Left, right HS cells' Vm (high-pass filtered, $Vm_{|5Hz}$) was projected onto a 2D side-view trajectory space for the left front leg's tibia-tarsus joint. Maps were constructed depending on whether the joint position at the stance onset was relatively more anterior (left, distant from the body) or posterior (right, closer to the body). Data from two example flies are shown. Red arrowheads indicate the approximate place of the stance onset. (**E**) Mean $Vm_{|5Hz}$ at the stance onset per fly when the tibia-tarsus (left, $p=0.0022$) or femur-tibia (right, $p=0.00025$, Wilcoxon signed-rank test, $n=19$ fly-cell pairs) joint was placed more anterior (light brown) or posterior (dark brown). A, anterior; D, dorsal; P, posterior; V, ventral.

Figure S4 (related to Figure 3): Simulations incorporating the relation between the forward velocity and HS-cell activity on a rapid timescale support the origin of stride-coupled neural modulations from the contralateral front leg

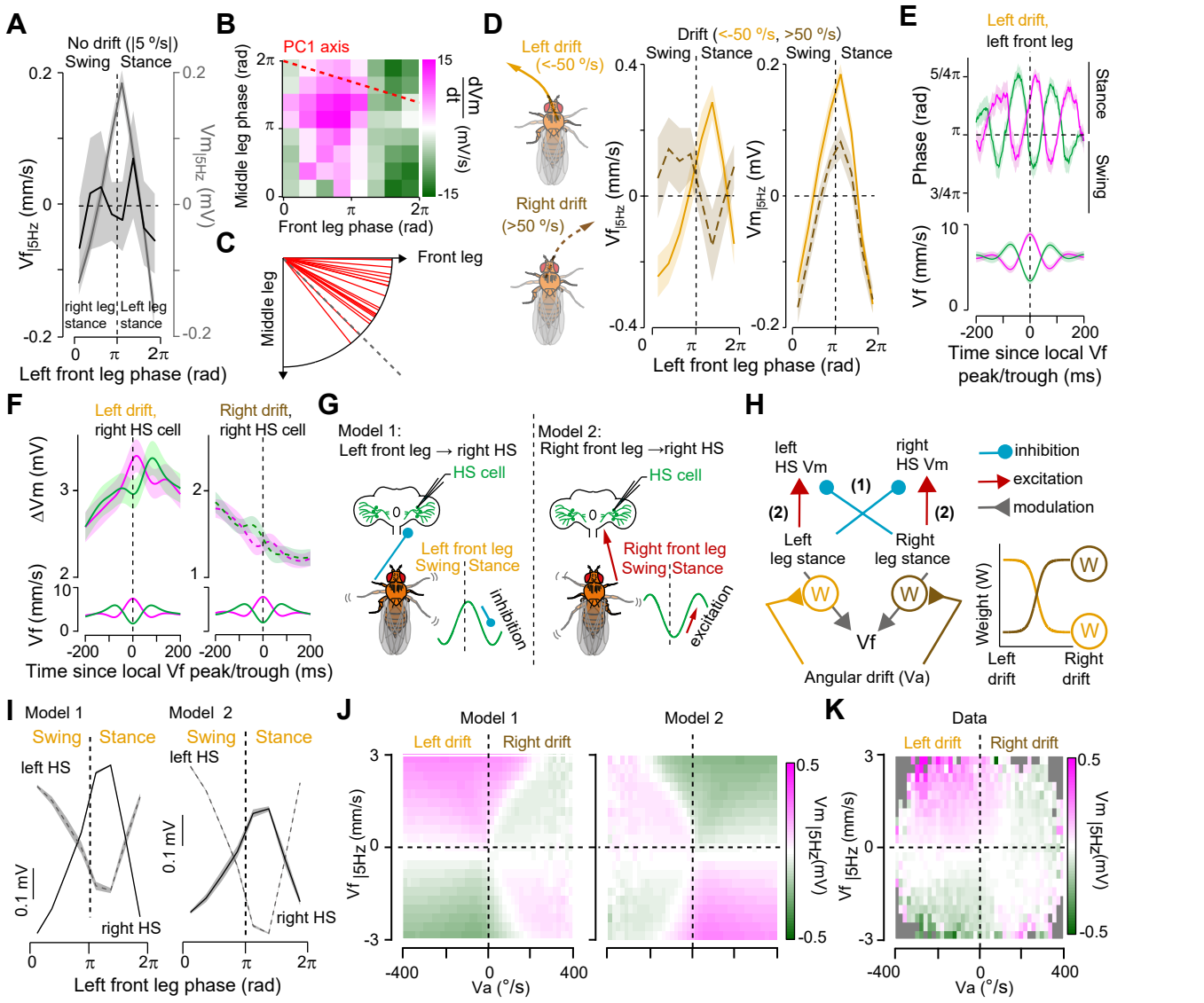

Figure S4 (related to Figure 3): Simulations incorporating the relation between the forward velocity and HS-cell activity on a rapid timescale support the origin of stride-coupled neural modulations from the contralateral front leg. (**A**) Tuning of Vf (high-passed filtered, $Vf_{|5Hz}$) and HS cells (high-passed filtered, $Vm_{|5Hz}$) to the stride cycle of the left front leg during opto-runs with marginal angular drift (-5<Va<5°/s; n=19 fly-cell pairs) (**B**) The temporal derivative of Vm of right HS cells (dVm/dt, from 19 cells) during opto-runs (see **STAR Methods**) projected onto a 2D leg-phase space; x-axis: left front leg, y-axis: left middle leg. The red dashed line indicates the PC1 axis of the 2D map. (**C**) PC1 axis calculated per fly-cell pair (n=19 pairs). The dashed line represents the alignment of the PC1 axis to both the front and middle legs. (**D**) Same as in (**A**) but for opto-runs with left (Va<-50 °/s, orange line) or right (Va>50°/s, maroon dashed line) angular drift (n=18 fly-cell pairs). (**E**) Left front leg phase (top) and Vf (bottom) triggered at the local peak (magenta) or trough (green) of Vf in opto-runs with left angular drift (n=18 fly-cell pairs). (**F**) Change in the activity of HS cells (ΔVm, top) and Vf (bottom) triggered at the local peak (magenta) or through (green) of Vf in spontaneous walking segments with left (n=23 fly-cell pairs, left) or right (n= 24 fly-cell pairs, right) angular drift. (**G**) Two models with different origin for the stride-coupled modulation in HS cells. In model 1, the contralateral front leg drives a hyperpolarizing signal during stance, whereas model 2 proposes a depolarizing drive from the ipsilateral front leg during stance. (**H**) Schematic of the circuit diagram for the simulation. Both right and left legs contributed to Vf with a weight (W) proportional to the ongoing Va, i.e., the direction of the fly's angular drift. (**I**) Simulated tuning of right (solid line) and left (dashed line) HS cells under models 1 (left) and 2 (right). n=50 simulated cells. (**J**) Simulated activity of right HS cells (high-pass filtered, $Vm_{|5Hz}$) as a function of the angular (Va) and forward (high-pass filtered, $Vf_{|5Hz}$) velocities of the fly based on model 1 (left) and model 2 (right). (**K**) Same as (**J**), but actual data (from 25 fly-cell pairs). All the traces show the grand mean ± SEM.

Figure S5 (related to Figure 4). Oscillations in Vm are reduced in flies with perturbed leg mechanosensory activity during periodic walking segments

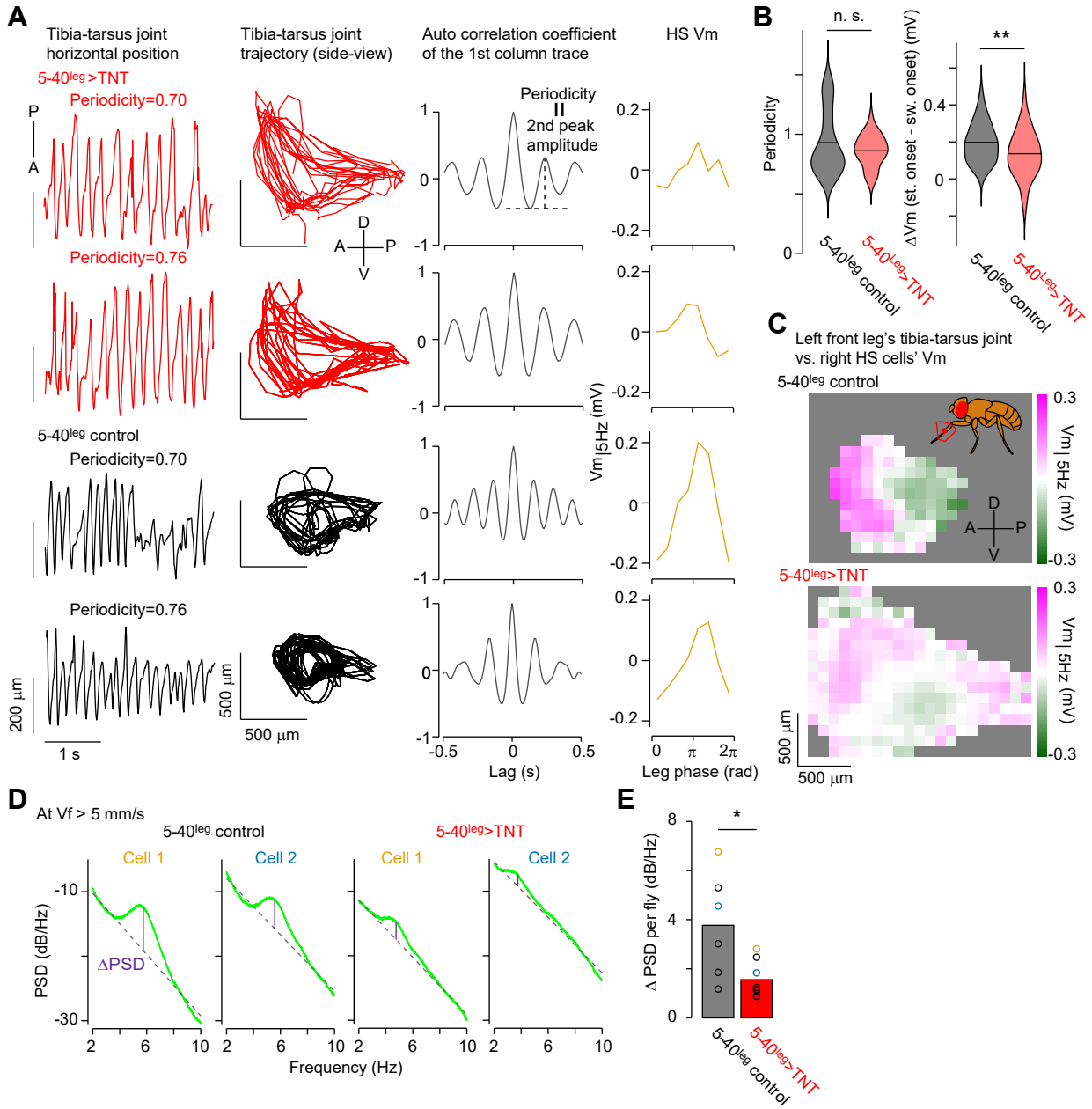

Figure S5 (related to Figure 4). Oscillations in Vm are reduced in flies with perturbed leg mechanosensory activity during periodic walking segments. (**A**) Examples time courses of the horizontal position (1st column) or 2D trajectory (2nd column) of the tibia-tarsus joint side-view trajectories (left front leg), the autocorrelation coefficient of the time series (3rd column), and $Vm_{|5Hz}$ tuning to the leg's stride cycle within the corresponding walking segment (3s, 4th column). Leg movement periodicity was calculated as the second peak amplitude in the autocorrelation coefficient trace. First and 2nd row, experimental flies (red, 5-40^{leg}>TNT); 3rd and 4th row, control flies (black, 5-40^{leg} control). A, anterior; D, dorsal; P, posterior; V, ventral. (**B**) Distributions of periodicity of the leg (left, p=0.62) and change in Vm (ΔVm) between stance and swing onsets (right, $p<10^{-5}$, Wilcoxon rank-sum test, n=208 (5-40^{leg} control, black) vs. n=149 (5-40^{leg}>TNT, red) walking segments. (**C**) Right HS cells' $Vm_{|5Hz}$ in experimental (top) or control (bottom) flies projected onto a 2D side-view trajectory space of the left front leg's tibia-tarsus joint. A, anterior; D, dorsal; P, posterior; V, ventral. (**D**) Power spectral density of Vm when the fly walked at high speed (Vf > 5 mms). Two example cells are shown for control (left) and experimental (right) flies. The strength of stride-related oscillations in Vm was defined as the difference (ΔPSD) between the local peak and the baseline (dashed line) of the PSD plot (see **STAR Methods**). (**E**) ΔPSD was significantly smaller for experimental vs. control flies (p=0.020, Wilcoxon rank-sum test, n=8 (experimental) and n=6 (control) fly-cell pairs).

Figure S6 (related to Figure 5). The excitability of HS cells over a stride strongly correlates with rapid steering independent of the state of angular velocity

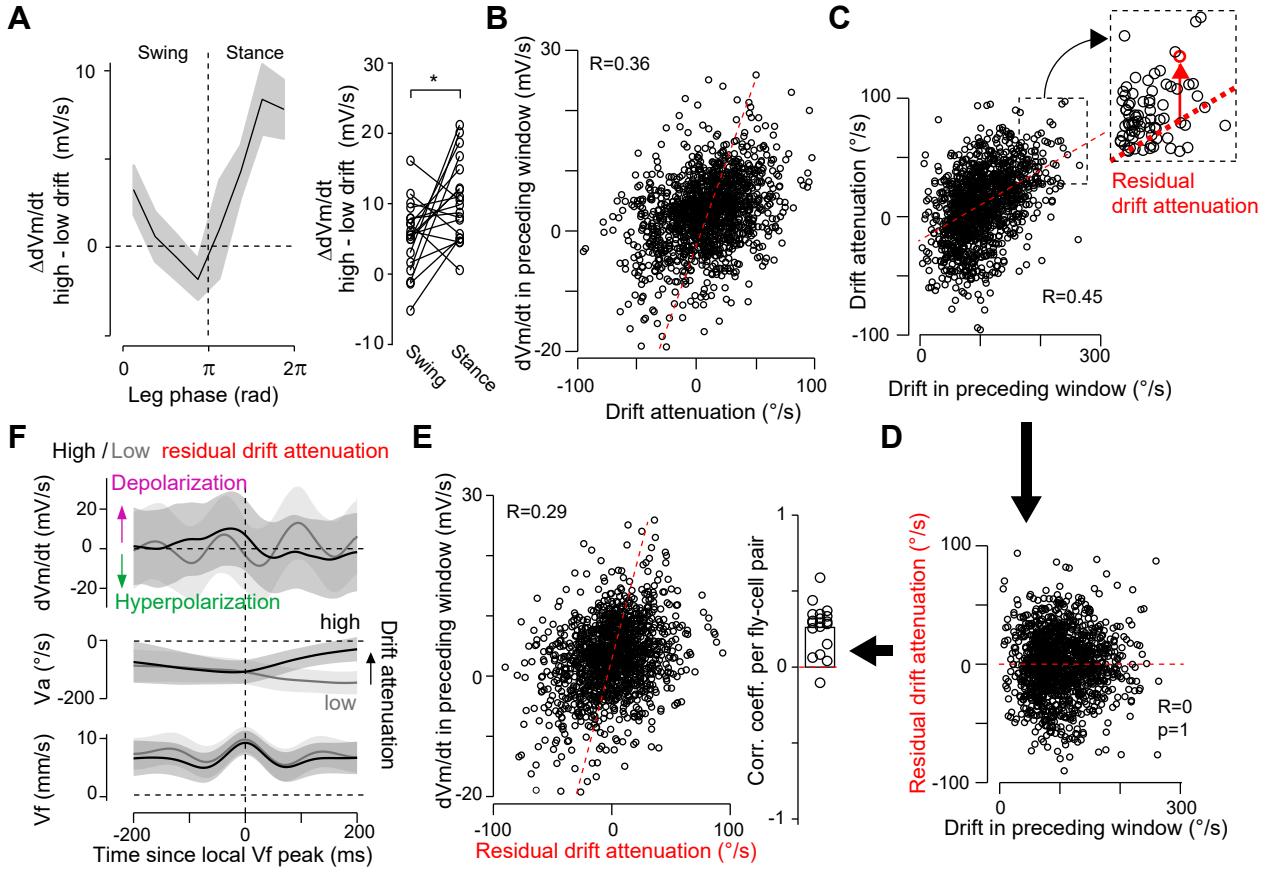

Figure S6 (related to Figure 5). HS-cell activity over a stride correlates with rapid steering independent of the state of angular velocity. (**A**) Left, the difference in HS cells' dVm/dt over a stride cycle of opto-run segments with low (-50°/s <Va<0°/s) vs. high (-200°/s<Va<-150°/s) angular drifts (ΔdVm/dt, see **Figure 5C**). Right, mean ΔdVm/dt per fly during swing vs. stance. Same individual connected by a line. The trace and shaded area represent the grand mean ± SEM, respectively (p=0.020, Z=-2.33, Wilcoxon signed-rank test, n=19 fly-cell pairs). (**B**) Mean temporal derivative of HS cells' membrane potentials (dVm/dt) per opto-run segment before the local Vf peak (time window: 200ms) vs. mean drift attenuation in the following 200ms. The dotted lines indicate the linear regression (R= 0.36, n=1378 segments from 19 fly-cell pairs). (**C**) Mean drift attenuation per opto-run segment over 200ms after the local Vf peak vs. mean angular drift per segment in the preceding 200ms (n=1378 segments from 19 fly-cell pairs). The dotted lines indicate the linear regression (R= 0.45). Inlet: definition of "residual drift attenuation" for an example data point (see also **STAR Methods**). (**D**) Mean residual drift attenuation per opto-run segment vs. the mean preceding angular drift over 200ms before the local Vf peak. The dotted lines indicate the linear regression (by definition, R=0, p=1). (**E**) Mean dVm/dt per opto-run segment over 200ms before the local Vf peak vs. mean residual drift attenuation in the following 200ms. The dotted lines indicate the linear regression (R=0.29). The right panel shows the correlation coefficient per fly-cell pair. The correlation was significantly positive (p=0.00025, z=3.66, Wilcoxon signed-rank test, n=19 fly-cell pairs). (**F**) dVm/dt (top), Va (middle) and Vf (bottom) triggered at the local Vf peak, in opto-run segments with similar magnitude of angular drift before the local Vf peak (leftward direction, Va<-50°/s), but with low (gray) or high (black) residual drift attenuation 200ms after the local Vf peak (n=360 segments; mean ± SD, segments were collected from 19 fly-cell pairs).

Figure S7 (related to Figure 7): Anatomy of LAL-PS-AN$_{contra}$, a class of ascending neurons projecting to IPS and LAL

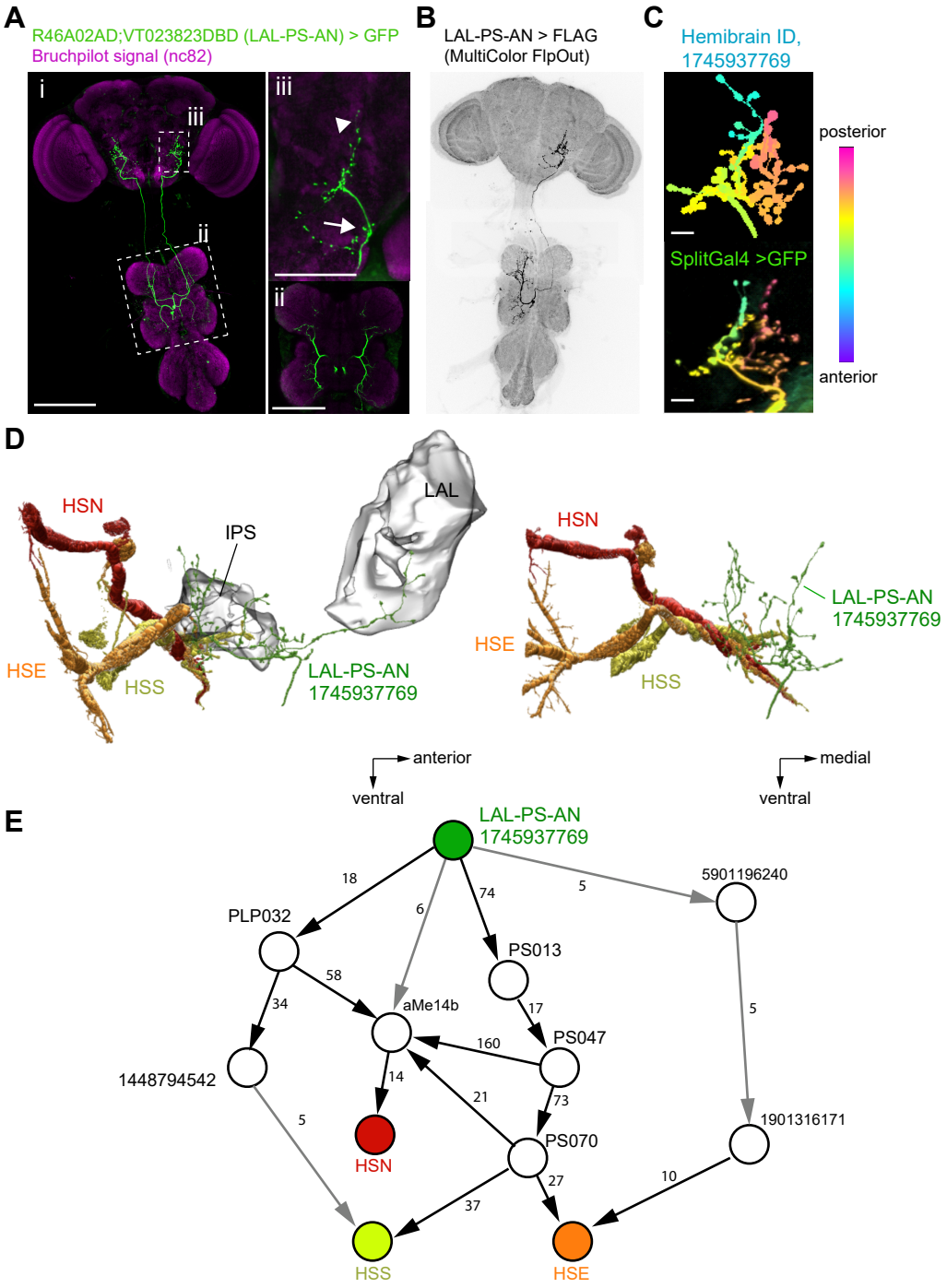

Figure S7 (related to Figure 7): Anatomy of LAL-PS-AN$_{contra}$, a class of ascending neurons projecting to IPS and LAL. (**A**) Projected z-stacked confocal image of the split-GAL4 line R46A02AD-VT023823DBD driving expression of EGFP (i). This line labels a class of ascending neurons that innervates leg neuropil within the proto- and mesomeres of the VNC (ii), and with brain projection fields within the gnathal ganglia (GNG), inferior posterior slope (IPS, arrow), and lateral accessory lobe (LAL, arrowhead) regions (iii). (**B**) A multi-color flip-out image revealing the contralateral projections of an individual LAL-PS-AN$_{contra}$. (**C**) Maximum intensity projection images (MIPs) of an aligned confocal image of our split-GAL4 (bottom) and a putative corresponding neuron identified in the hemibrain EM dataset. Color represents different frames of the image stack in the antero-posterior axis. (**D**) EM-based reconstructed HS cells and the putative LAL-PS-AN$_{contra}$ neuron (green) from the hemibrain dataset (see **STAR Methods**). (**E**) Shortest possible path between the putative LAL-PS-AN$_{contra}$ neuron and HS cells. Synaptic weights: ≥5 synaptic contacts, gray; ≥10 synaptic contacts, black. Scale bars: 100 µm (**A, B**); 10µm (**C**).

Figure S8 (related to Figure 8): Relationship among the stance duration, forward velocity, and left HS-cell activity

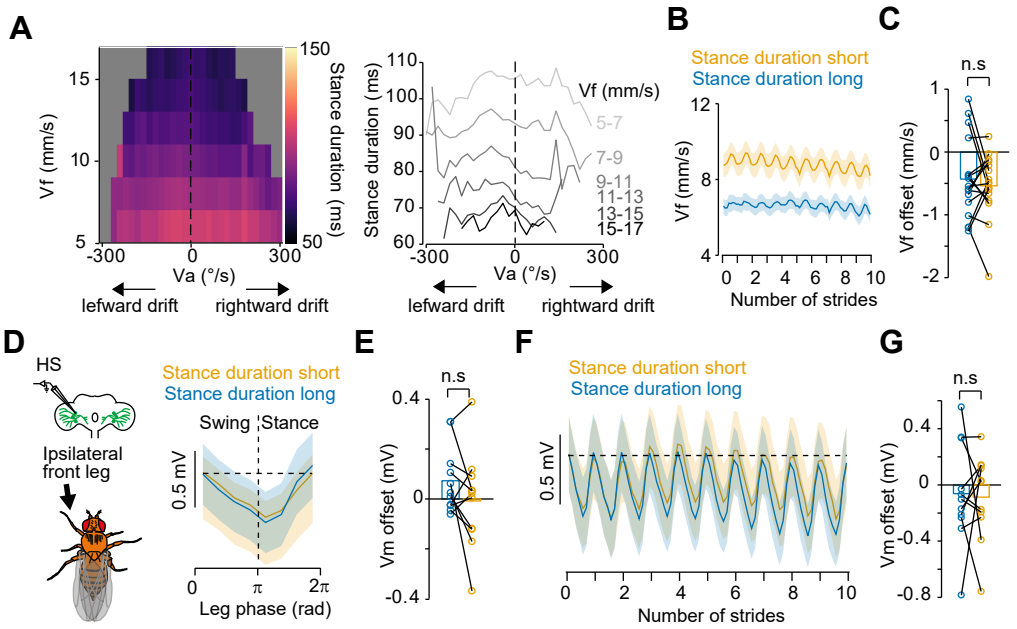

Figure S8 (related to Figure 8): Relationship among the stance duration, forward velocity, and left HS-cell activity. (**A**) Left, front leg stance duration as a function of the angular (x-axis, Va, 20 °/s bins) and forward (y-axis, Vf, 2 mm/s bins) velocities of the fly. Right, the mean stance duration as a function of Va at different Vf. Data were collected from 19 flies. (**B**) Vf tuning to the left front leg stride cycle over ten strides for shorter (orange) or longer (blue) stance duration (grand mean ± SEM, n=17 flies). (**C**) The Vf offset at the end of ten strides relative to the beginning for shorter and longer stance durations (p=0.62, Z=0.50, n=17 flies, Wilcoxon signed-rank test). (**D**) Left, schematic of the experimental configuration. Right, left HS cells tuning to the left front leg phase for shorter (orange) or longer (blue) stance durations (grand mean ± SEM, n=11 fly-cell pairs). (**E**) The Vm offset at the end relative to the beginning of the stride for shorter and longer stance durations (n=11 fly-cell pairs, p=0.28, Wilcoxon signed-rank test). (**F**) Same as (**E**), but traces over ten strides. (**G**) Same as in (**E**) but for ten consecutive strides (p=0.97, n=11 fly-cell pairs, Wilcoxon signed-rank test).